Casting Shadow on the Photocatalytic Activity of Plasmonic Antimony Doped Tin Oxide Nanoparticles in Degrading Rhodamine 590

by

Enas Howsawi

A thesis

presented to the University of Waterloo

in fulfillment of the

thesis requirement for the degree of

Master of Science

in

Chemistry-Nanotechnology

Waterloo, Ontario, Canada, 2018

Author's Declaration

I hereby declare that I am the sole author of this thesis. This is a true copy of the thesis, including any required final revisions, as accepted by my examiners.

I understand that my thesis maybe made electronically available to the public.

Abstract

Increasing the feasibility of water purification systems at the manufacturing, technical and material engineering level is an urgent matter that is of global interest. Concerning materials engineering for water purification *via* water splitting, numerous studies have been done to match the ever-increasing demand in that field and finding new economically feasible solutions. A way to achieve lower cost and higher efficiency is to switch from the highly delicate processing procedures of thin films to nanostructured materials prepared by solution-based method. For that purpose, nanomaterials have specifically shown remarkable activity when studied under ultraviolet illumination. Indeed, utilizing UV as an excitation source for photocatalysis has its drawbacks since UV radiation constructs only about 5% of the solar radiation, making many of the studied systems inefficient unless an artificial UV source is present. One solution presented in this thesis is engineering a system that can utilize the most abundant portion of the solar radiation: the infrared (IR) radiation. However, the challenge remains because IR radiation is very low in energy and cannot excite valence band (VB) electrons through the band gap (Eg) for most nano-systems. In this regard, a successful IR photocatalytic study relies upon finding a suitable candidate with adjustable parameters to work efficiently under IR excitation.

Antimony doped tin oxide (ATO) was selected as a model system that can respond to IR excitation by absorbing IR energy and stimulating a collective oscillation of conduction band (CB) electrons. Materials with such a feature are often referred to as plasmonic and the frequency that matches the incident IR resonance is called local surface plasmon resonance (LSPR). Given that IR radiation is also associated with thermal emission based on Black Body Radiation Theory, the LSPR electrons in ATO are supposedly responsive to thermal emission from their surrounding medium.

The deliberate incorporation of antimony atoms into the matrix of SnO_2 is a fundamental component in creating a plasmonic system. Greenish ATO nanoparticles (NPs) grow darker in color upon increasing the dopant concentration which is attributed to the increasing population of CB. In this system, Sb^{5+} played the main role in increasing the CB occupancy whereas Sb^{3+} had an adverse effect on the free electron population. When the NPs were subjected to high temperatures below the melting point of ATO, the color turned bluish indicating a higher electron density in the CB.

The photocatalytic activity of moderately doped samples did not always demonstrate a thermal-IR response. The results marked the importance of freeing-up the surface sites for incoming dye molecules, in this case Rhodamine 590 (Rh-B). Aside from having a small surface area, annealing highly doped ATO samples allowed them to perform the photocatalytic reaction by successfully employing their LSPR property. The small surface area is an undesirable feature in photocatalytic studies but in this circumstance, it served as a confirmation that the degradation of the dye is not adsorption related. However, further annealing beyond 600℃ can negatively impact the photocatalytic reaction by increasing antimony occupation of the surface and limiting the sample's activity to adsorption. This underlines the importance of the treatment conditions. For further elucidation of thermal-IR response, the temperature of the studied medium was modified several times to draw a correlation between thermal activation and degradation rate. It is important to mention that samples labeled as photocatalytically inactive were not able to show such correlation which further confirmed the conceptual hypothesis.

The mechanism of Rh-B degradation *via* thermal-IR activation was elucidated from the results of scavenger experiments. The degradation reaction was suppressed using an electron scavenger, emphasizing the role of electrons in the degradation process and further supporting the argument of thermal-IR activation. Also, there was a clear difference between the photocatalytic activity of active 12% doped ATO annealed at 600℃ and inactive as-synthesized SnO_2 and 6% doped ATO annealed at 800℃. Remarkably, the photocatalytic activity of the latter two samples under UV was found to be suppressed in the presence of a hole scavenger.

These results demonstrate the possibility to design and control the plasmonic properties of metal oxide NPs to perform a photocatalytic reaction at the desired temperature and with the use of IR spectral range. In broad vision, this work is expected to stimulate future research on IR and plasmon-related photocatalytic studies.

Acknowledgements

First, I'd like to express my gratitude and appreciation to my supervisor Dr. Pavle Radovanovic for his assistance in building fundamental knowledge and substantial skills. He always displayed extensive knowledge and an undeniable passion for science. His guidance, remarkable comments and help to develop self-dependence were key factors in the success of this work. My gratitude also goes to my committee members Dr. Vivek Maheshwari and Dr. Anna Klinkova for taking the time to read and make insightful comments on my thesis.

This work wouldn't have been completed without the contribution from so many individuals. Many thanks to Dr. Carmen Andrei, Dr. Sardar Ayub, and Andrew Kacheff for their assistance in acquiring the TEM images, XPS and BET data. My gratitude is extended to Dr. Howard Siu and Dr. Chun Xia for being so accommodating with cold pressing my samples and performing the FTIR measurement. I also want to state my gratefulness for Dr. Yousef Abu-Nada from the Saudi Cultural Bureau who was constantly available for professional advice. Lastly, I would like to acknowledge the Klinke group for helping with XRD data collection.

My sincere appreciation is expressed to all current and previous group members to whom I owe a lot for making my work successful. I first thank Terry for his contribution to my training; especially during my early days in the group. I would also like to thank Natalie for creating a very accommodative environment and making insightful comments during my work. I'm specifically grateful to Vahid who exhibited a massive experience and knowledge and was always available to support and answer questions with patience and respect. I also had the privilege to work closely with Susi, Manu, Yunyan, Baran, Joshua, Jonathan, Chen, Yi, Paul, Nathaniel, Wenhuan and Hanbing with whom I consistently had valuable discussions. All of the Radovanovic members expressed friendly attribute and displayed excellent teamwork and the character of true scientists.

Also, I would like to show my appreciation for all of the amazing friends with which God blessed me. Each one of them was fundamental in making my stay in Waterloo enjoyable and fruitful.

My genuine regards for my parents and siblings for their continuous support throughout my master’s degree. Special thanks for my brother and best friend Owais who always stood by me in difficult times. His encouraging words were what kept me going.

I wouldn’t have come this far without you all…

Thanks…

Table of Contents

List of Figures

List of Tables

List of Abbreviation

ATO	Antimony Doped Tin Oxide
BA	Anhydrous Benzyl alcohol
BET	Brunauer–Emmett–Teller
CBM	Conduction Band Maximum
Cyc.hex	Cyclohexane
Eg	Band Gap
FTIR	Fourier Transform Infrared
FWHM	Full Width at Half-Maximum
HR	High Resolution
Iso.pro	Isopropanol
LSPR	Local Surface Plasmon Resonance
MeOH	Methanol
MIR	Mid Infrared
NC	Nanocrystal
NHE	Standard Hydrogen Electrode
NIR	Near Infrared
No scav.	No Scavenger
NP	Nanoparticle
OlAm	Oleylamine
PCE	Perchloroethylene
Rh-B	Rhodamine 590
RT	Room Temperature
TCO	Transparent Conducting Oxide

TEM	Transmission Electron Microscopy
UV-Vis	Ultraviolet-Visible
VBM	Valence Band Maximum
XPS	X-Ray Photoemission Spectroscopy
XRD	Powder X-ray Diffraction

Chapter 1

Introduction to Plasmonic Photocatalysis and Plasmonic ATO

1.1. Overview of LSPR's fundamentals and utilities

1.1.1. Background Information of LSPR theories

The field of material science plays a major role in the establishment and development of new theories that can enhance the performance of modern technology. One of the most studied subjects around the globe is water splitting for the purpose of water purification and hydrogen production. A class of materials being utilized in water splitting, known as transparent conducting oxides (TCOs), exhibit the unique property of having a high electrical conductivity while maintaining a high transparency in the visible region of the electromagnetic spectrum. The high conductivity originates from the presence of different types of defects that can increase the electron density and create an n-type semiconductor. As for the transparency feature, it comes from the large band gap of this type of materials, which is at least 1.3 eV.[1]

The density of defects in TCOs can be empirically manipulated by different procedures such as introducing foreign atoms to the host lattice of the material. Indium oxide (In_2O_3) and tin oxide (SnO_2) are n-type semiconductors that are commonly doped with various elements, including tin, zinc, aluminum and antimony using different implantation methods.[1] One of the features that distinguish indium and tin oxide systems from other TCOs is their ability to exhibit a local surface plasmon resonance (LSPR) phenomenon that makes them useful for a wide range of commercial applications.[2]

The concept of LSPR, which was first introduced in 1857, corresponds to the oscillative movement of free electrons that is restricted to the surface of the material in response to an incident electromagnetic wave.[3, 4] The electron's collective oscillation results in an electric field of specific frequency, which if matched the frequency of the incident electromagnetic wave, will be called a plasmon resonance.[4] This type of behavior is exclusive to materials in the nano-scale and has been observed in noble metals and certain types of semiconductors as well.[5] In order for a certain material to show an LSPR feature, the size of the nanoparticle (NP) must be smaller than the wavelength of the incident light and the electron mean free path.[3]

Figure 1.1 is a schematic illustration of the excited plasmon state and small dipole moment created inside the NP. The absorption and scattering of light is largely enhanced at the frequency of plasmon resonance which is readily related to the concentration of free carriers in the conduction band (CB) according to Equation 1.1, where ω_p, N_e, e, ε_∞ and m^* represent the plasmon frequency, concentration of free carriers, electron charge, permittivity of free space and the electron effective mass inside the CB. In a typical LSPR behavior, the absorption peak that corresponds to LSPR blue shifts and grows higher in intensity upon increasing the carrier density while it exhibits the inverse trend when the electron density decrases.[2] Moreover, the high concentration of free carriers in the CB outlines one of the main differences between noble metals

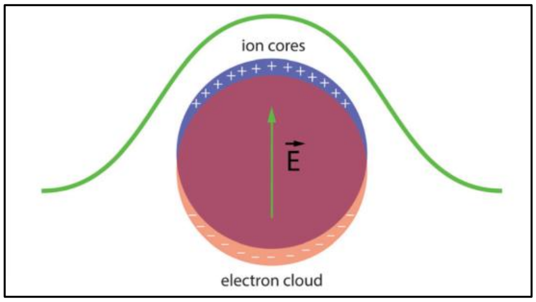

Figure 1.1. Schematic illustration of LSPR phenomenon in NPs. The green arrow indicates the rise of a restoring force as a result of the displacement of the electron cloud (orange area) that moved away from the positive centers (blue area).[2]

$$\omega_p = \sqrt{\frac{N_e\, e^2}{\varepsilon_\infty\, m^*}} \tag{1.1}$$

and doped semiconductors and allows LSPR applications of noble metals to operate at higher energies. It is also worth mentioning that the variation in electron density between metallic and semiconductor systems provides a broader range of frequencies in which LSPR is active.[6]

The Mie's Theory, in 1908, is one of the earliest work that explained the interaction between electromagnetic wave and spherical NPs. Up to date, the theory is still valid, and people employ it to infer the correlation between scattering cross section and photon energy. Other relations and parameters can then be withdrawn such as the linewidth of the LSPR mode.[6, 7] The theory is particularly useful in demonstrating the dependence between the plasmon resonance and the surrounding medium of spherical NPs. Figure 1.2 (a) and (b) display the relation between the refractive index of the surrounding medium and LSPR photon energy. If the dielectric constants of the NP and the surrounding medium are known, one can infer the position of the LSPR

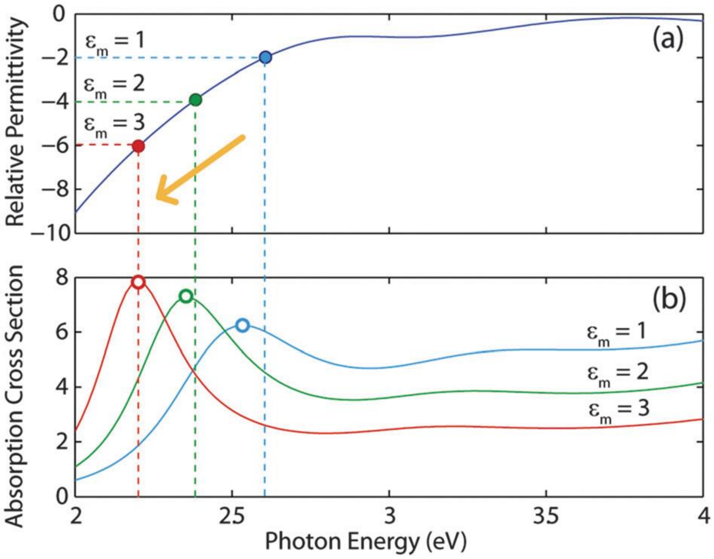

Figure 1.2 Graphical illustration of the relation between photon energy and LSPR surrounding medium. (a) The intersection of $-2\varepsilon_m$ with the axis of relative permittivity of gold NCs. (b) Calculated absorption spectra of gold nanocrystals (NCs). The correlation between the two panels is demonstrated by the dashed lines.[6]

mode by graphically intersecting a horizontal line with the relative permittivity axis. The line must be drawn at $-2\varepsilon_{m}$, where ε_{m} corresponds to the dielectric constant of the surrounding medium.[6] The empirical observation for this correlation is the position of LSPR maximum absorption in the electromagnetic spectrum. This in overall suggests a high sensitivity of the LSPR mode toward its surrounding medium.

Thereafter, different models have been developed to deal with some of the shortcomings of the Mie's Theory. For examples, Maxwell and Garnett' model was designed to take into consideration the close packing of LSPR NPs. In another model, polarizability has been presented as the oscillation direction in the transvers and longitudinal mode concerning the different shapes of NPs.[8]

The Drude model that is usually applied in LSPR studies, accounts for the carrier mobility and damping of the resonance by various collision mechanisms according to Equation 1.2 and

$$\varepsilon = \varepsilon_{m} - \omega_{p}^{2} / (\acute{\omega}^{2} + i\gamma\omega) \tag{1.2}$$

$$\gamma = e / (\mu m^{*}) \tag{1.3}$$

1.3, in which ε, $\acute{\omega}$, i, γ and μ are the permitivity of the, NC the cross-over frequency, the imaginary number , the damping parameter and the mobility of the free carriers respectively. Typically, scattering has a more pronounced effect because the size of the NPs is relatively smaller than the mean free path of the eletrons which leads to large collision events with the surface. Surface scattering may lead in some cases to a slight shift of the plasmon band if the crystallite size reaches very minute sizes of 3 nm and smaller. Therefore, according to Equation 1.3, increasing the carrier mobility or mass may minimize the damping effect. However, this part of the theory is hard to fulfill when doped semiconductors are involved.

At high doping concentrations, the scattering events will happen more frequently due to collision with implanted impurities and defects leading to an inevitable adverse effect on carriers' mobility.[6] This challenge was discussed in the theory of electron gas oscillation in plasma which stated that the damping's integral becomes negligible once the mean free path becomes largely bigger than the wavelength of the incoming light.[9] That is to say, in practice, one should aim for a moderate concentration of electrons at a low dopant concentration to reduce the damping effect. In general, LSPR can be observed in NCs larger than a couple of a nanometer and smaller than one fifth of the wavelength of the incident electromagnetic wave that triggers the LSPR phenomenon.[6]

Moreover, the carrier density of CB free carriers is quantitatively correlated with the absorption coefficient (α_e) of free electrons through modified Drude-Lorentz model. In the expression

$$\alpha_e = \frac{N_e\, e^2}{m^*\, \varepsilon_\infty\, n\, c\, \tau\, \omega^2} \tag{1.4}$$

n is the refractive index, c is the speed of light, τ is the mean free time between two colliding electrons and ω is light frequency.[10]

Last, from the standpoint of the relation between LSPR absorption peak and the behavior of free electrons in the lattice, various studies have demonstrated the possibility to numerically deduce the electron mobility, mean free path and relaxation time from FTIR results. Also, the scattering mechanism can be studied based on the carrier's optical mobility ($\mu_{L_{opt}}$) in Equation

$$\mu_{L_{opt}} = \frac{e}{2\, \alpha_p\, \omega_0\, m^*} \left[\exp\left[\frac{\hbar\omega_0}{K\,T}\right] - 1\right] \tag{1.5}$$

1.5 , where α_p is the polaron coupling constant, $\hbar$ is reduced Planck's constant, ω_0 is the frequency of the longitudinal optical phonon, K is Boltzmann's constant and T is the absolute temperature.[11] The electrons mean free path (l) within grain boundaries is given by the formula

$$\mathrm{l} = \left(\frac{\mathrm{h}}{2\ \mathrm{e}}\right)\left(\frac{3\ \mathrm{N_e}}{\pi}\right)^{1/3} \mu_{\mathrm{L_{opt}}} \qquad (1.6)$$

and is usually utilized to infer the scattering mechanism. h in Equation 1.6 corresponds to Planck's constant.[12]

1.1.2. LSPR classifications and properties

LSPR NCs can be classified into three main categories according to the mechanism of which their free carrier's density is created; namely, self-doped systems, extrinsically doped and metallic systems. In the first category, the carrier density results from the non-stoichiometry of implanted atoms, which exist in different oxidation states. In order to retain charge balance, extra electrons or holes are donated to the CB or the valence band (VB) respectively.[6]

In the second category, there is a fixed number of electrons and defects in the material, and the LSPR mode is triggered by doping the system with foreign atoms or *via* other protocols that can improve the carrier density. [6] For example, a lattice may accommodate new dopant atoms by removing the original ions from their stationary equilibrium positions. This will result in charge imbalance, and to preserve charge neutrality, the extra electrons will be donated to the CB. The key factor for the first and second category is to make a proper selection of chemicals and the preparation procedure in order to reach the desired number of free carriers.

As for the last category, metals exhibit a fixed number of free carriers and high conductivity due to the continuity of their oxidation sates. An example of this type of materials is noble metals.[6]

There are many parameters that govern the LSPR feature of NPs beside the concentration of free carriers, and the color of plasmonic NCs is one prevalent character to start with. LSPR NCs are normally colored due to the absorption of certain frequencies in the visible light and reflection of the complementary colors. For example, gold NCs appear red-purple due to the absorption of the green region of the spectrum. The same concept applies to yellow silver NCs that absorb in the blue region of the spectrum at 400 nm.[4] The color is strictly related to the real part of the dielectric constant, the permittivity of the surrounding medium and the NC size.[13]

In addition, the shape of the LSPR band is another fundamental parameter that is impacted by NC size. The damping of LSPR in large NCs is dominated by non-radiative decay leading to a broad LSPR absorption band in the spectrum.[5] Moreover, separate absorption bands may appear according to the shape of the NC and polarization direction. For instance, gold NCs with a nanorod shape were reported to exhibit two distinct absorption bands in the visible region. The longitudinal polarization mode appeared at the longer wavelength side while the transverse mode showed up at shorter wavelengths.[14]

Lastly, the dielectric constant of the surrounding medium is one effective parameter that can influence the position of the LSPR peak, as has been stated in the previous section. Mahmoud et. al, reported a systematic shift of the LSPR peak of silver NCs dispersed in different solvents. The peak position was observed to red shift when increasing the refractive index of the medium.[15] In another study, the LSPR peak of copper oxide NPs was observed to shift by changing the pH for the same salt solution, confirming that LSPR's absorption and scattering processes are medium sensitivite.[16]

1.1.3. LSPR applications

The carrier density of noble metals is a fixed parameter and normally falls in the range of 10^{23} cm^{-3} which limits their application to the visible and ultraviolet (UV) part of the spectrum. Improved functionality can be reached by using doped LSPR semiconductors, which can operate at lower energies in the infrared (IR) region. The carrier density in these materials is far less than noble metals; nevertheless, semiconductors have the privilege of tunable electron concentration and operational region.[17] For instance, some LSPR NCs can be used in near-IR (NIR) catalytic reactions for gas detection.[13, 17] They also find use in medical treatments like biosensing and in improved optical response of smart windows.[2, 4, 5, 18] More recent studies observed a photoluminescence signal enhancement due to LSPR and increased fluorescence intensity due to energy transfer from plasmon to fluorophore particles.[19, 20, 21]

1.2. Evolution of photocatalysis from conventional into plasmonic

1.2.1. Conventional photocatalysis

Water splitting through photocatalytic reactions for hydrogen production and complex organic compounds degradation has been extensively explored using a wide range of materials. It is true that using powder catalysts in practical photocatalytic applications has not been realized yet; however, that doesn't undermine the big advancement in powder photocatalytic studies. In order for a certain system to be photocatalytically active, its CB has to be more negative than the

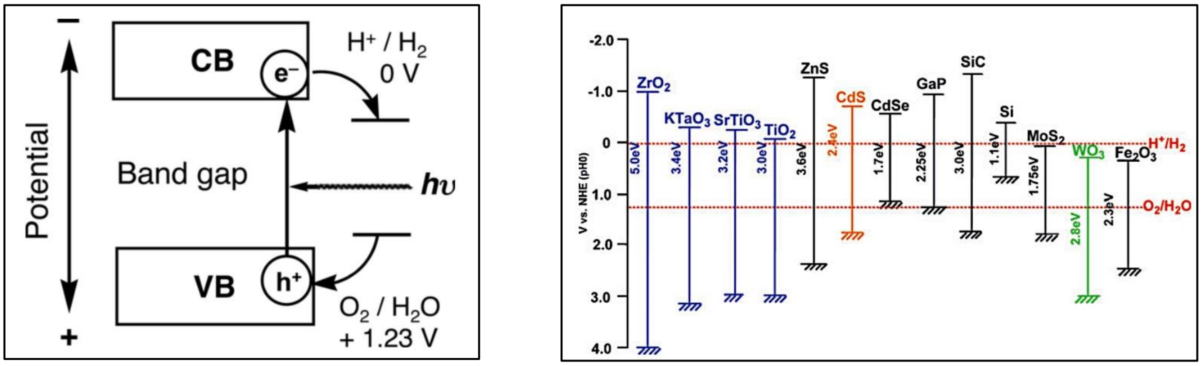

(a) **(b)**

Figure 1.3. (a) Schematic illustration of water splitting reactions *via* photocatalysis. The CB and VB positions represent the ideal case scenario for this type of reactions, while the two lines on the right side of the figure indicate the presence of defect states. (b) Review of popular photocatalytic systems in water splitting reactions. Each system shows a certain deviation from the ideal case for the CB and VB potentials.[22]

standard hydrogen electrode (NHE) reduction potential, and the VB has to be more positive than NHE oxidation potential. When an electromagnetic wave with energy higher than the catalyst's band gap strikes the surface of the catalysts, it stimulates the excitation of an electron to the CB leaving a hole behind it in the VB. Figure 1.3 (a) illustrates the typical photocatalytic steps for water splitting. It is possible for a certain system to undergo only one set of catalytic reactions depending on the alignment of its band gap with NHE potentials. Figure 1.3 (b) reviews some of the famous systems in water splitting reactions and demonstrates their band gap alignment with respect to NHE.[22]

Water splitting can result in direct production of hydrogen and oxygen molecules or in the creation of certain reactive radicals that can participate in the degradation of organic pollutants by breaking their chemical bonding. Generally, $2H^+$ can accept an electron from the CB and form H_2. Also, a hydroxyl radical (OH^-) may accept a hole from the VB and form OH.[23]

The photocatalytic process is often affected by different parameters that can increase, decrease or in some cases completely hinder the catalytic reaction. One of these parameters is the presence of sacrificial agents, often referred to as scavengers, that can capture the photogenerated electrons and holes or react with the created reactive species from water splitting. In addition, the presence of defects inside the band gap has an important contribution because defects can capture the photogenerated charge carriers and either positively or negatively influence the degradation rate. Lastly, the surface area of the catalyst plays an important role in the adsorption of organic molecules on the surface of the catalyst at the early stages of the photocatalytic reaction.[22]

Hitherto, most of the known catalysts operate only in the presence of a high energy source such as a UV light. This quite limits the practicality of the photocatalytic reaction, especially since UV rays construct only about 4% of the solar spectrum.[24, 25]

1.2.2. Plasmonic photocatalysis

1.2.2.1. Advantages of plasmonic photocatalysis

Research work on plasmonic photocatalysis was first initiated in the 21st century in order to increase the efficiency of the photocatalytic reaction and find more compatible solutions for water purification with lower energy sources.[26] It was previously stated in Section 1.1.1. that the shift of the electron cloud creates a small restoring force inside the NPs and concurrently a local electric field in the opposite direction of the dipole. Once the resonance of the incoming light couples with that of the plasmon, it will lead to an enhanced absorption, scattering and electric field. The enhanced electric field in particular can result in an improvement of the photocatalytic process by boosting the generation of charge carriers.[3, 26]

Besides enhancing the local electric field, LSPR phenomenon can lead to a local heating effect that improves the photocatalytic reaction rate. Collision events that take place between electrons and phonons and among phonon modes result in increasing the temperature of the local environment around the NPs. The heating effect may vary from one system to another, and although the heating process normally lasts for only a few hundred picoseconds, it can significantly modify the temperature of the medium to a degree of 3 to 5 $°C\ S^{-1}$.[26]

Last, the diffusion length of the exciton still plays an essential role in the rate of the photocatalytic reaction. Short diffusion length can lead to rapid recombination between photogenerated carriers and hence adversely impact the degradation rate of organic pollutants.[3]

1.2.2.2. Review of LSPR systems used in photocatalysis

Up to date, most of the known LSPR photocatalytic systems still require the presence of a noble metal oxide to serve as a plasmonic source. Normally, a semiconductor will be embedded into a proper noble metal and a junction is formed between the two materials.[21, 27, 28, 29, 30, 31]

The shift from metal-semiconductor conjunctions to pure plasmonic semiconductors in photocatalysis is still a developing field with little exploration. Since the reported semiconductors in plasmonic systems are mainly metal oxide, it is relevant to give a special attention to lattice defects, especially since most metal oxide semiconductors are known to form natural structural defects. It is also common knowledge that the photocatalytic activity of semiconductors may be hindered in the presence of a large amount of defects, and one possible way to eliminate structural defects is to anneal the sample under certain conditions. Newman and his coworker stated that active defect centers can cause light absorption in sub-band gap states. These deep defect states were successfully deactivated in their work *via* thermal annealing at high temperatures. It is worth to mention that the defects were subject to reactivation upon further annealing.[32] In a different study, Tull et. al illustrated that annealing the semiconductor system can lead the dopant ions to build up at grain boundaries and thus prevent efficient absorption of certain electromagnetic wavelengths.[33, 34]

Overall, the selection of a good candidate for LSPR photocatalysis may include a semiconductor that is classified as TCO, has a relatively small band gap, displays a reasonable alignment with NHE and can be easily modified to exhibit an LSPR feature. These categories can quite fit a number of group d^{10} metal cations, such as In^{3+}, Zn^{2+}, Cd^{2+} and Sb^{5+}.[22, 35] It also fits Sn^{4+} cation, the first commercialized TCO, which was chosen to be the focus of the current study.[1]

1.3. Tin oxide in photocatalysis

SnO_2 is an n-type semiconductor, with a rutile crystal structure, tetragonal unit cell and a band gap equals 3.6 eV.[35, 36] The material exists in nature in the form of Cassiterite mineral and exhibits the symmetry $P4_2/mnm$, with a = b = 4.738 A° and c = 3.188 A°. Sn element can display two oxidation states of Sn (II) and Sn (IV) which allows it to take in the form of different stoichiometric metal oxides; however, all of the other forms will eventually convert into the more stable SnO_2 stoichiometry. It's possible for SnO_2 to be a p-type semiconductor and in that case the effective mass of the hole is quite large and can reach about $\sim 1\mathrm{m_o}$, note that the electron effective mass in an n-type SnO_2 is in the range of $0.25\mathrm{m_o}$.[35]

Further illustration of n-type and p-type conductivity is depicted in Figure 1.4 (a) and (b).

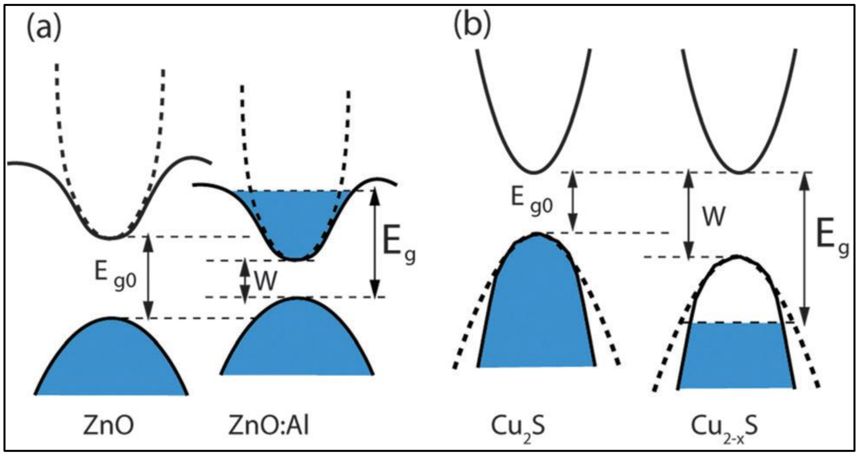

Figure 1.4. Representation of Burstin-Moss effect in semiconductors. (a) The Eg expands due the increased density of negative charge carriers in the CB. (b) The Eg shrinks due to the increased density of positive charge carriers in the VB. Eg_0 is the band gap value of a non-doped semiconductor. Eg is the modified band gap value, often called effective band gap. W refers to the difference between the top of the VB and the bottom of the CB.[6]

These two cases are examples of a Burstein-Moss effect of band gap widening and shrinking. The original band gap remains unchanged, but the addition of electrons or holes to either the CB or the VB modifies the effective band gap respectively. In example (a), the optical band gap value of Aluminum doped Zinc oxide extends to include the additional occupied energy levels of the CB created by the extra electrons from the doped atoms. In case (b), extra holes were created in the VB of deficient Copper Selenide and the optical band gap value decreased accordingly.[6]

The main reason that makes SnO_2 n-type conductive is the presence of free carriers in the CB due to oxygen vacancies ($V_o^{\cdot\cdot}$) and Sn interstitials (Sn_i). Oxygen vacancies form when an

$$O_o^X \rightarrow V_o^{\cdot\cdot} + 2\,e' + 1\,/\,2\,O_2\,(g) \tag{1.7}$$

oxygen atom sequentially leaves its crystal position, creates one vacancy in its original place and releases two electrons into the unoccupied levels of the CB. The defect states of oxygen vacancies are located below the minimum of the CB; whereas, the defect levels of Sn interstitials exist inside the CB, which makes the latter a more effective source for conductive free carriers.[35]

SnO_2 is often doped with higher valence elements, such as Sb^{5+}, in order to improve its conductivity.[35] Antimony is incorporated into the lattice by replacing Sn^{4+} atoms in their crystal position as either Sb^{5+} at low dopant levels or as a mixture of Sb^{5+} and Sb^{3+} at high dopant concentrations.[37] Sn^{4+} ionic radius = 0.69 and Sb^{3+} = 0.76 A° which makes hosting the coordination (III) less favorable when compared to Sb^{5+} with the ionic radius of 0.60 A°.[1, 35] To further illustrate, the following two equations demonstrate the aforementioned scenarios of antimony atoms entering SnO_2 lattice.[38]

$$Sb_2O_3 \overset{SnO_2}{\rightarrow} 2\,Sb_{Sn}' + V_o^{\cdot\cdot} + 3\,O_o \tag{1.8}$$

$$Sb_2O_5 \overset{SnO_2}{\rightarrow} 2\,Sb_{Sn}^{\cdot} + 2e' + 5\,O_o \tag{1.9}$$

The color of antimony doped tin oxide (ATO) powder is normally yellowish and converts to brown, green and eventually blue upon annealing the sample at a high temperature. The color change is a direct indication of the material conversion to n-type conductivity due to the increased free carriers in the CB. This behavioral change is reflected on the optically detected LSPR peak in the IR region.[1, 37] The blue color of ATO samples was observed to stay for more than one month indicating a good stability of the activated LSPR phenomenon.[1] Nevertheless, some papers reported a low conductivity of ATO NPs at very high dopant concentrations and with post-annealing treatments. From their perspective, these observations are attributed to either the creation of a p-type conductivity, due to increased incorporation of Sb^{3+} coordination, or the trapping of free carriers in deep defect states.[37, 39, 40] ATO studies have also stated that Sb^{3+} forms shallow acceptor levels close the VB, and Sb^{5+} introduces shallow donor levels close to the CB.[41, 42] When more dopants are introduced, the activation energy of Sb^{5+} donor states moves upward and creates more lattice disorder and scattering events.[42]

To construct a photocatalytic experiment using powder catalysts, people often dissolve a colorful organic dye in water to represent water pollutants in nature. The photocatalytic study initiates by the organic compound's adsorption on the surface of the dispersed catalyst in water. Next, the medium is illuminated to stimulate redox reactions. In many studies, SnO_2 in the pure and co-doped form has proven to be an effective material for the degradation of a wide range of organic compounds under UV and visible light irradiation.[36, 43, 44, 45, 46] It is important to add that $^{\bullet}O_2^-$ and $^{\bullet}OH$ radicals were found to be the most effective species when SnO_2 system is used in the degradation experiment and in spite of the type of the organic dye.[47, 48]

$$SnO_2 + hv \rightarrow h^+_{(VB)} + e^-_{(CB)} \tag{1.10}$$

$$h^+_{(VB)} + H_2O \rightarrow {}^{\bullet}OH + H^+ \tag{1.11}$$

$$e^-_{(CB)} + O_2 \rightarrow {}^{\bullet}O_2^- \tag{1.12}$$

$${}^{\bullet}O_2^- + H^+ \rightarrow HO_2{}^{\bullet} \tag{1.13}$$

$$HO_2^{\bullet} + H^+ \rightarrow H_2O_2 \tag{1.14}$$

$$\text{Dye} + {}^{\bullet}OH \rightarrow \text{Degradation products} \tag{1.15}$$

$$\text{Dye} + {}^{\bullet}O_2^- \rightarrow \text{Degradation products} \tag{1.16}$$

$$\text{Dye} + H_2O_2 \rightarrow \text{Degradation products} \tag{1.17}$$

Proposed degradation mechanism can be summarized in the equations from 1.10 to 1.17.[48, 45]. Equation 1.10 represents the initial step of charge carrier creation. Equations 1.11 to 1.14 involve the production of active free radicals that are responsible for the degradation process. The last three equations from 1.15 to 1.17 vary from one study to another depending on the photocatalytic system involved and the most active species to participate in the reaction. It is important to note that SnO_2 has also been used in plasmonic photocatalysis using a conjunction of Ag/SnO_2 and Au-SnO_2, under visible light irradiation.[49, 50, 51] Besides, non-plasmonic ATO NPs were also studied in the degradation of phenol under solar light irradiation.[52]

On a final note, Rawal et. al, have attempted to use dark-blue plasmonic ATO NPs in photocatalysis back in 2011 using a conjunction of ATO, TiO_2 and CdSe. The position of the CB and VB of ATO in their study prevented the plasmonic electrons from reaching their full potential and the system was only utilized for VB hole transfer from TiO_2 to ATO. Nonetheless, a remarkable question has been raised about the fate of accumulated ATO CB electrons induced by visible light absorption. Nonetheless, no correlation was made between the decomposition of the studied gas and the plasmonic property of ATO in the conducted experiments.[53]

1.4. Reported ATO synthesis techniques

Different synthesis techniques have been employed to prepare ATO NCs in the powder and thin film form. The techniques for the latter ranged from coprecipitation, spray pyrolysis, magnetron sputtering, spin casting, solvothermal and sol-gel; just to name a few. [42, 54, 55, 56, 57,58] On the other hand, there was far less reports about the synthesis of plasmonic ATO NPs in the solid form; namely, chemical coprecipitation and sol gel. Besides, an additional post-annealing step at high temperature was usually a requirement to activate the LSPR mode, otherwise, the powder is a non-plasmonic dark yellow material or a barely green product with low carrier concentration.[59, 60, 61] Up to the present time, the best reported procedures to produce dark green to navy blue ATO NPs with LSPR property are the work done by Min and Bao in 2008 utilizing a self-assembly combustion technique and that published by Xu and his colleagues in 2015 using a hydrothermal method.[62, 63] A replication of the hydrothermal procedure will be employed in the current study.

1.5. IR photocatalysis

IR radiation constructs half of the solar energy, and yet, efficient catalysts that can utilize IR radiation in water splitting are still to be found. The challenge originates from the difficulty to find a good candidate that can achieve enough IR response and has a band gap with a reasonably good alignment with NHE. The first communication letter to report a photocatalytic water splitting study using IR radiation was published in 2015 by Cui and his coworkers. In their work, they made a conjunction of WO_2–Na_xWO_3 in order to stimulate the photocatalytic reaction as illustrated in Figure 1.5. In this study, the IR driven photocatalytic study included three steps. At first, IR radiation creates an electron and hole pairs in the CB and VB of WO_2 respectively. The induced free carrier in the CB stimulate the reduction reaction of water and create H_2 molecules. Secondly, another electron hole pair is created in Na doped WO_3. The hole forms in the introduced defect states of Na and the electron in the CB transfers to the VB of WO_2. In the final stage, a third electron is excited to the defect states of Na, and a new hole is created in the VB of Na_xWO_3. The location of valence band maximum (VBM) allows for the utilization of VB holes in the oxidation reaction and yields water molecules. It can be clearly seen that this study has directly related the photocatalytic activity of the semiconductor system to IR radiation.[64]

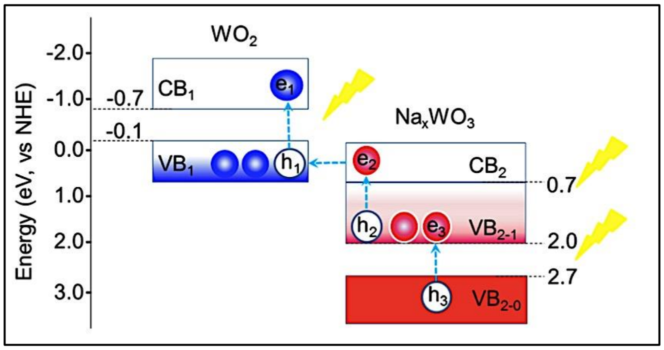

Figure 1.5. Energy level diagram for LSPR $WO_2 – Na_xWO_3$. The VB created by Na addition to WO_3 is responsible for initiating the oxidation process and producing h^+. Whereas the reduction process occurs by the subsequent transfer of e^- to the CB of WO_2.[64]

From a different viewpoint, IR radiation is related to thermal radiation. According to Black-Body Radiation Theory, all bodies emit a thermal radiation at a temperature above 0 °C due to energy transfer at the electronic, atomic and molecular level. This type of emission occurs between 0.1 to 100 μm, with the majority of it falling in the IR region, as shown in Figure 1.6. The amount of thermal energy emitted at a certain frequency corresponds to a specific type of electromagnetic wave that is deduced from Planck's law in Equation 1.18. $E_{b\lambda}$, λ, T, C_1, C_2 are the

$$E_{b\lambda}(\lambda, T) = \frac{C_1}{\lambda^5\left[\exp\left(\frac{C_2}{\lambda T}\right) - 1\right]} \qquad (1.18)$$

emissive power of the black body, the wavelength of the radiation, the absolute temperature of

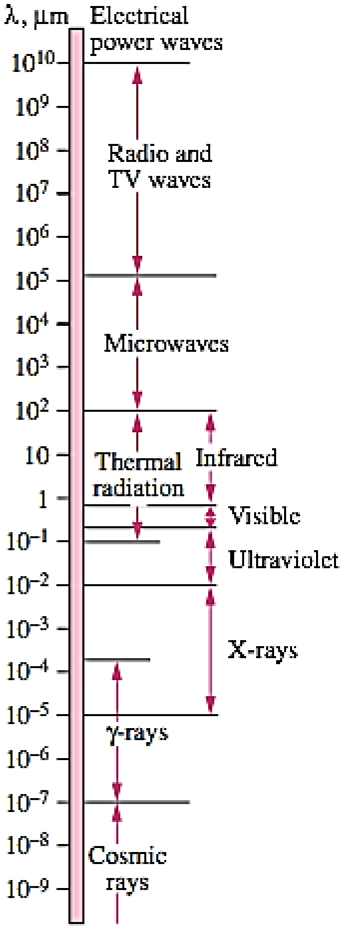

Figure 1.6. Schematic diagram of the electromagnetic wave spectrum. Thermal radiation corresponds to the IR and visible radiation and includes a small portion of the UV region.[65]

the radiating surface, a constant equals 3.742×10^8 W μm^4 m^{-2} and a constant equals 1.439×10^4 µm K respectively. Plotting the relation between the emissive power and emission wavelength in Planck's relation yields the scheme presented in Figure 1.7. The dashed line in the scheme follows the shift of the emission maximum intensity for each corresponding temperature according to Wien's displacement formula.[65]

$$(\lambda\ T)_{\text{max power}} = 2897.8 \qquad (1.19)$$

Based on the aforementioned relation between IR and thermal emission, one can utilize the thermal radiation from a certain aqueous medium as an IR radiation source to perform an IR photocatalytic study. Therein, it will be more accurate to refer to the conducted study as thermal-IR photocatalysis.

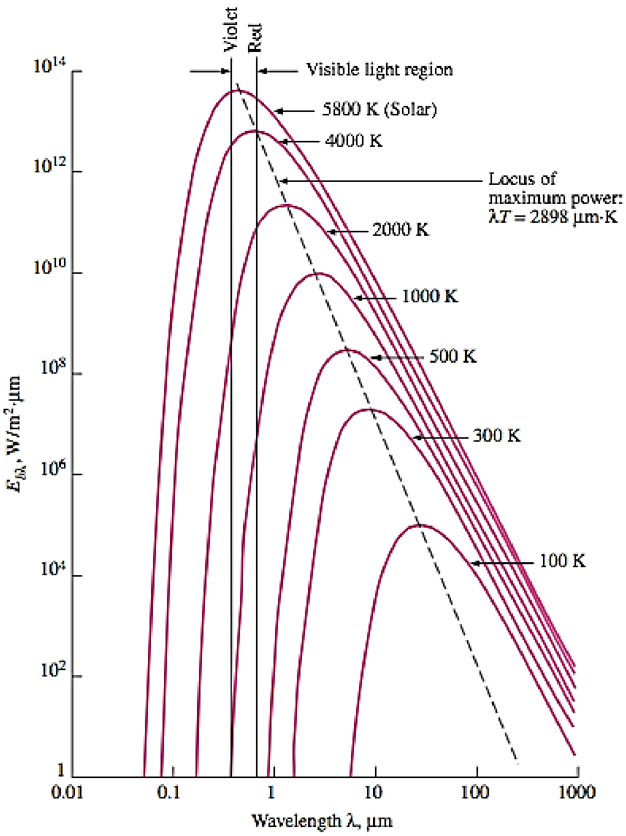

Figure 1.7. Schematic representation of the relation between emissive power and wavelength over a wide range of surface temperatures for an ideal blackbody. The dashed line passes through the center of the thermal curves' maximum emissive power (max power).[65]

1.6. Motivation and scope of the thesis

Since plasmonic photocatalysis in the IR region is still limited to one single study done three years ago, and no work has since been done on thermal-IR photocatalysis, there is a need to explore this novel field and cast a shadow on the mechanisms and properties behind it.

This project is divided into three parts that mainly cover the study of ATO plasmonic NPs. The first part provides an in-depth analysis of the physiochemical environment, LSPR feature, electrical properties of ATO NPs using different instrumental techniques and numerical calculations. This part of the project is expected to add to the overall understanding of ATO's LSPR behavior in the solid form, which can facilitate the use of ATO NPs in different plasmonic applications.

The second part of the project focuses on studying the plasmonic photocatalytic activity of ATO NPs. In this part, various experimental conditions were modified once at the time in order to link the observed trends with what has been reported about plasmonic photocatalysis. Concurrently, the observed behavior was correlated with the results obtained from ATO optical and electrical analysis and are expected to pave the way for more studies of a similar nature.

The last part of the project aims to elucidate the degradation mechanism and confirm some of the hypotheses made at the early stages of the work. The experiments performed in this part of the project involved the use of various scavengers that are often employed to decide the limiting steps in the photocatalytic degradation process.

LSPR NCs are seldom utilized in a single field of technology as has been demonstrated earlier in Section 1.1.3 of this thesis. Each LSPR research is expected to contribute to the overall understanding of LSPR phenomenon and draw the attention to the important impact of certain parameters.

Chapter 2

Experimental Details

2.1. Materials

Anhydrous Antimony (III) trichloride ($SbCl_3$; 99%), Anhydrous benzyl alcohol (BA; 99.8%), oleylamine technical grade (OlAm; 70%), cyclohexane (Cyc.hex; 99%), Titanium (IV) oxide anatase (TiO_2; 99%), perchloroethylene (PCE; 99%) and Rhodamine 590 (Rh-B) were all purchased from Sigma-Aldrich. (Acetone; 99%) and Tin (IV) tetrachloride pentahydrate ($SnCl_4 \cdot 5H_2O$; 98%) were purchased from Fisher Scientific. The chemicals were used as received without any further purifications.

2.2. Synthetic procedure

The synthesis method employed in this project replicates the same procedure outlined by Xu and his coworkers.[63] A series of ATO samples was made by changing the content of antimony precursor in the reaction. The starting concentrations were made so that the molar concentration of [Sb/Sn] equals 1, 4, 6, 10, 12 and 20%, donated by ATO-1, ATO-4, ATO-6, ATO-10, ATO-12 and ATO-20 respectively. In a typical reaction procedure, 0.0019 molar of $SnCl_4$ was added to the desired molar of $SbCl_3$ in a round bottom flask. 30 ml BA was then added to the reaction medium at room temperature (RT) and the solution was vigorously stirred for half an hour. Afterward, the solution was poured into a 40 ml teflon aligner. The sealed autoclave was then transferred to a preheated oven at 200 °C, and the reaction was hydrothermally treated for 24 hours. The obtained product was separated from the oil phase by centrifugation at 5000 rpm for 10 minutes. The precipitate was then washed three times with acetone and left to dry on a watch glass. Pure SnO_2

sample was also made following the above-mentioned steps without adding $SbCl_3$. Once the precipitates were dry, they were grounded and made into powder for XRD and photocatalytic experiments.

To perform further optical measurements, colloidal samples were prepared by dissolving 0.1 g of the dried powder in 20 ml perchloroethylene with the addition of 10 drops of oleylamine.

Also, to improve the plasmonic feature of the samples and perform further photocatalytic experiments under better conditions, dried SnO_2 and ATO samples were annealed for two hours at different high temperatures; namely, 400 ℃, 600 ℃ and 800 ℃. Annealed samples were later grounded into powder again for different analysis.

2.3. Characterization techniques

2.3.1. Transmission electron microscopy (TEM)

TEM is a transmission technique that involves detecting a transmitted electron signal to formulate a picture of the sample.[66] TEM is typically used to adequately find the real crystallite size, study the morphology of the NCs, find the preferred lattice orientation and find the real dopant concentration and element distribution *via* elemental mapping. In this study, TEM measurement was conducted at McMaster University using a JEOLL-2010F microscope that operates at 200 kV. The samples were prepared by depositing a few drops of the colloidal solution on a lacey Formvar/carbon support film of a copper grid using a micropipette. The grids used here were purchased from TedPella, Inc.

One of the challenges associated with ATO samples scanning in this study was to get a clear image of the surface of the samples. The presence of oleylamine ligand in the solution made the images blurry by absorbing the light and preventing it from transmitting through the sample. Therefore, the colloidal samples were remade again by only dispersing the NPs in cyclohexane and sonicating them for 10 minutes. A few drops were immediately taken from the murky solution and dropped on the TEM grids before allowing the NPs to rest back to the bottom of the vial. The second challenge was the overlap between antimony and tin ionization energy, which prevented the utilization of the full instrumental capacity, and hindered the characterization of elemental composition.

2.3.2. *Powder x-ray diffraction (XRD)*

XRD is a powder diffraction technique often used to prop the predominate crystal structure of the corresponding lattice and detect any impurities and secondary phases. XRD measurement was performed using an INEL XRD diffractometer in Dr. Holger Kleink's lab in the Chemistry department at the University of Waterloo. The instrument uses a monochromatic radiation of Cu-K_α radiation (λ = 1.5406 A°).

Parameters such as the mean crystallite size can be extrapolated from XRD data. Debye Scherrer equation is used to calculate the effective crystallite size (δ) as stated in Equation 2.1, where k is Scherrer constant, λ is the wavelength of utilized X-ray radiation, $\beta_{1/2}$ is

$$\delta = \frac{k\,\lambda}{\beta_{1/2}\cos\,\theta} \tag{2.1}$$

the full width at half-maximum (FWHM) of the diffracted peak of X-ray radiation taken in radians and θ is the corresponding degree of the diffracted peak. $\beta_{1/2}$ is extracted from Gauss multiple fitting of (110) reflection.

2.3.3. *Ultraviolet-visible (UV-Vis) spectroscopy*

UV-Vis-NIR is a spectroscopic technique that can be used to determine the band gap of pure and doped semiconductors based on light absorption and transmission. Moreover, the technique is also utilized in detecting the presence of LSPR feature and finding about its corresponding free carrier concentration. With this technique, it is possible to modify the detection parameters to include part of mid-IR (MIR) region. In the UV measurement of this thesis, samples were made ready for UV-Vis scanning by drop casting the transparent colloidal samples on a quartz substrate. The scanning was run from 200 – 3300 nm to cover the whole range from UV to MIR. As for the optical band gap, it was extrapolated from the Tauc plot of $(\alpha_e \, E)^2$ *vs* E, using Equation

$$(\alpha_e \, E)^2 = X\,(E - E_g) \qquad (2.2)$$

2.2 for direct band gap semiconductors.

Furthermore, UV-Vis is also used in photocatalytic studies to record changes in the organic dye level and determine the degradation rate. The dye final concentration in the solution is extrapolated using Beer−Lambert law of A/A_0 where A and A_0 represent the final and starting absorbance respectively. The equation is usually modified to C and C_0 so that it respectively correlates to the final and starting concentration of the dye. As for the starting concentration, it’s determined by the point at which adsorption and desorption reactions reach equilibrium. [67]

The apparent degradation rate (k_{app}) is another parameter that is extrapolated by linearly fitting ln C_0/C to the degradation time (t) according to Langmuir−Hinshelwood model of

$$\ln \frac{C_0}{C} = k_{app}\, t \qquad (2.3)$$

Equation 2.3 assuming a pseudo-first order kinetic.[67] Equation 2.4 represents the formula used in determining the percentage of degraded dye.

$$\frac{C_0 - C}{C_0} \times 100 \qquad (2.4)$$

In this project, 25 mL of 5 mg^{-1} L Rh-B was added to a 100 mL beaker and was then mixed with 6 mg of the catalyst. Rh-B characteristic peak at 520 nm was used to evaluate the dye concentration. In the part of the study where UV light is involved, the beakers were situated 20 cm away from the light source and the power of the two fluorescent tube lamps was 40 W filtered at 254 nm.

2.3.4. *Fourier transform infrared (FTIR) spectroscopy*

FTIR is a typical technique for detecting LSPR feature in Mid-IR and the presence of organic molecules in the lattice. It is a specialized technique that can work as a finger-print of individual systems because it detects vibrations and transitions at the molecular level.[68] Hence, samples were made ready for the measurement by making Nujol-molls from acetone and powder samples. Then the Nujol-molls were spread as thin films over a solid KCl disk. Subsequently, a second KCl solid plate was placed on the exposed side of the sample and scanned with FTIR in the transmission mode. The scanning range was taken from 400 to 4000 cm^{-1} using a Bruker tensor 37 in the undergraduate lab of the chemistry department.

2.3.5. *Brunauer–Emmett–Teller (BET) surface area analyzer*

The BET measurement is designed to find the surface area of the studied material using an inner gas adsorption-desorption isotherm.[69] The sorption isotherms are then fitted to a BET equation to obtain the specific surface area information. In this study, the BET study was done in Dr. Prouzet’s group using a Quantachrome Autosorb instrument. The measurement was performed at 77 K using nitrogen as the carrier gas.

2.3.6. *X-ray photoemission spectroscopy (XPS)*

XPS is a powerful tool that can yield detailed information at the atomic and electronic level and allow for adequate determination of the band structure and oxidization states. In the current study, pelletized samples were examined with XPS at the University of King Fahad for Petroleum and Minerals in Saudi Arabia. The experiments were performed in a Thermo Scientific Escalab 250 Xi spectrometer that utilizes Al Kα (1486.6 eV) as a monochromatic X-ray source. During the scan, the chamber was flooded with an electron gun to avoid charging of samples and a pressure of about 10^{-9} was maintained for the whole duration of the experiment.

A 200 mg of the powder samples were cold pressed to obtain 12 × 0.7 mm circular pellets. Although pelletized samples extend the duration of the experiment, they are particularly useful in avoiding inhomogeneous surface charging and champers's pressure's fluctuation when the samples out-gas during the experiment.

Chapter 3

Primary Spectroscopic Analysis

3.1. Structural study of ATO

3.1.1. Physical characterization of color evolution

ATO NPs were hydrothermally prepared at 200 ℃ for 24 hours following the steps described in Chapter 2 Section 2.2. The visual color of ATO samples plays a crucial role as a primary indicator of the plasmonic property of the system. In general, the development of a greenish to bluish color is a visual indication of the formation of an n-type conductivity in the prepared NPs.[70] The color intensity also indicates an improvement in the CB's electron concentration.

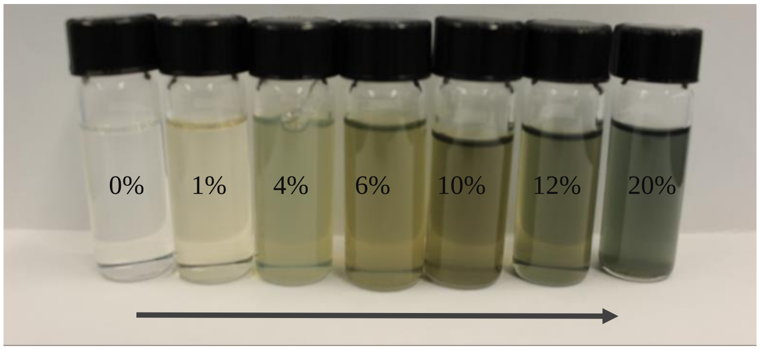

Figure 3.1. Digital photo of as-synthesized ATO samples in their colloidal form. The samples were dispersed in cyclohexane mixed with a few drops of oleylamine. The colors get more intensified upon increasing the dopant concentration indicating an increased free carrier concentration.

From Figure 3.1, it is evident that the samples start to develop a more intense greenish color with the increase of antimony concentration. ATO-12 imparts blue coloration after annealing the sample at 800 ℃ whereas ATO-6 800 tends to slightly loose its green coloration as illustrated from the pelletized samples in Figure 3.2. ATO-12 and ATO-6 are selected as good representatives for high and low dopant concentrations and will be used for any future in-depth analysis and studies in this project.

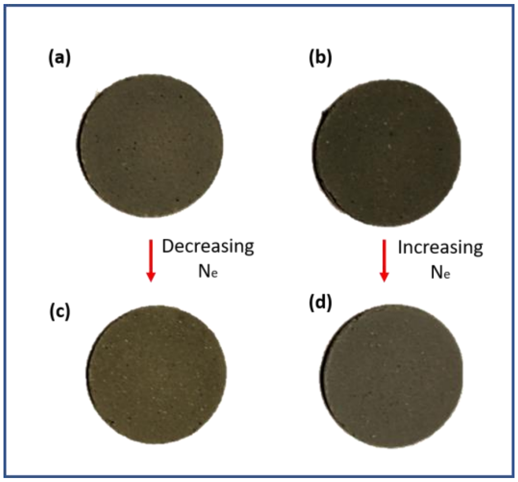

Figure 3.2. Digital picture of pelletized ATO samples that demonstrates the greenish to bluish color transition. (a) ATO-6 600. (b) ATO-12 600. (c) ATO-6 800. (d) ATO-12 800.

3.1.2. *Morphological and structural overview via TEM*

The presence of chlorine ions can lead to the agglomeration of the NPs and create some lattice inhomogeneity.[59] Thus, TEM was used to test the as-synthesized SnO_2 NPs dispersed in

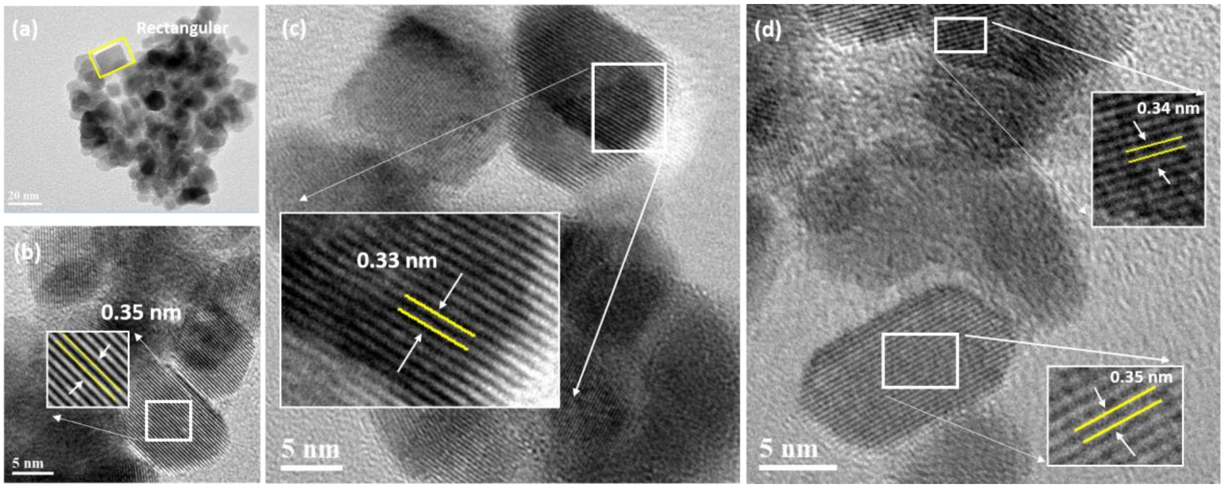

Figure 3.3. Representative TEM image of as-synthesized SnO_2 NPs. (a) Overview image of the sample's morphology. The HR-TEM micrographs from different regions on the grid show a lattice spacing of (b) 0.35 (c) 0.33 and (d) 0.34 nm from a tetragonal, cubic and hexagonal morphology respectively. All values correspond to SnO_2 (110) lattice plane and are indicated by yellow lines. The white rectangles specify the exact position where the lattice spacing was calculated.

cyclohexane murky solution. Based on Figure 3.3 (a), pure SnO_2 exhibits various morphologies ranging between rectangular, hexagonal and cubic lattice ordering. The high resolution (HR-TEM) micrograph images from Figure 3.3 (b) to (d) indicate the crystalline nature of the obtained product with the lattice fringes corresponding to the interplanar distance of (110) lattice plane.[71] Different areas were scanned and the lattice spacing in all regions agrees well with the standard value of SnO_2 (110) lattice plane for a tetragonal crystal structure. The apparent crystallite size ranges between 20 to 15 nm in the longitudinal direction of the rectangular and hexagonal lattices and is generally 10 nm in width.

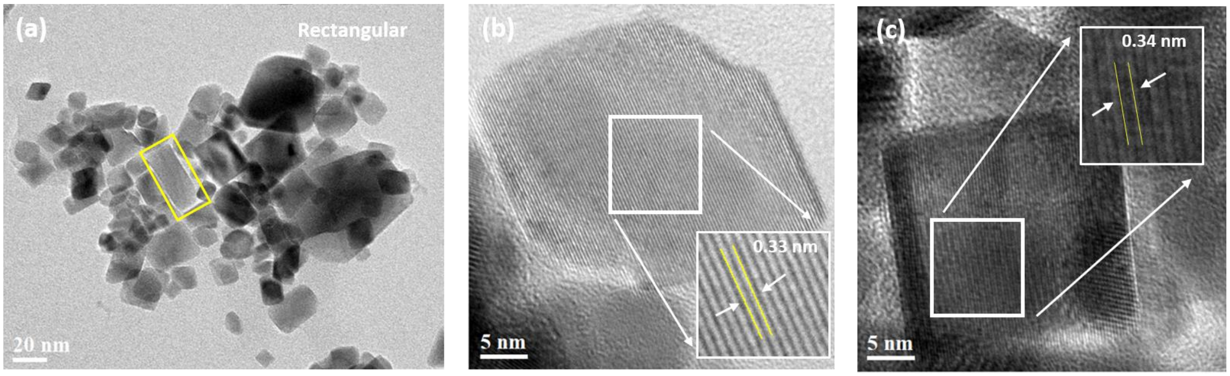

Figure 3.4. Representative TEM images of as-synthesized ATO-12 NPs. The overview image in (a) displays the different morphological structures of the lattice. The HR-TEM images show a lattice fringes of (b) 0.33 and (c) 0.34 nm from a pyramidal and cubic morphology respectively. The lattice fringes agree with the standard spacing of SnO_2 (110) lattice plane. The white rectangles specify the exact position where the lattice spacing was calculated.

ATO-12 was also examined with TEM to provide a good comparison of pure and doped samples and a representation of the effect of antimony incorporation on lattice morphology. Aside from the detected pyramidal shapes, the overview images in Figure 3.4 (a) indicate that doping SnO_2 lattice with antimony doesn't have a large impact on the lattice ordering with the three morphological structures still present in the sample. No apparent impact on the crystallite's size is detectable, and (110) lattice plane remains the preferable growth direction as indicated from the calculated lattice spacing in Figure 3.4 (b) and (c). No 0.35 nm interplanar spacing was detected in the studied specimen which implies a tendency to have a shorter atomic spacing driven by tin atoms substitution by antimony.[69] An overall implication from the images is that antimony atoms are likely well accommodated into SnO_2 lattice sites. Hence, the overlap between tin and antimony energy peaks hinders the evaluation of the real incorporation of the foreign atoms into the host lattice.

3.1.3. *Evaluation of phase purity via XRD*

XRD was performed to analyze the purity of the phase and study the structural orientation of the crystallites. The results from as-synthesized and post-treated samples match the diffraction peaks of tetragonal cassiterite SnO_2 (JCPDS 88-0287). It is clearly seen from Figure 3.5 (a) to (d) that there are no unidentified reflections which indicates the absence of any secondary phases. It is relevantly important to mention that various reports on ATO NPs reported a successful accommodation of up to 30% antimony dopant in the cassiterite structure with no secondary phase formation.[60, 72] The aforementioned observation indicates that doping SnO_2 cassiterite lattice with 20% antimony is still within the solubility limit.

There is an observable gradual increase in the diffracted peaks' intensity and sharpness upon annealing the samples at 600 and 800 ℃, and that can be corresponded to an improved crystallinity that enhanced the signal coming from certain diffraction points. The plotted results

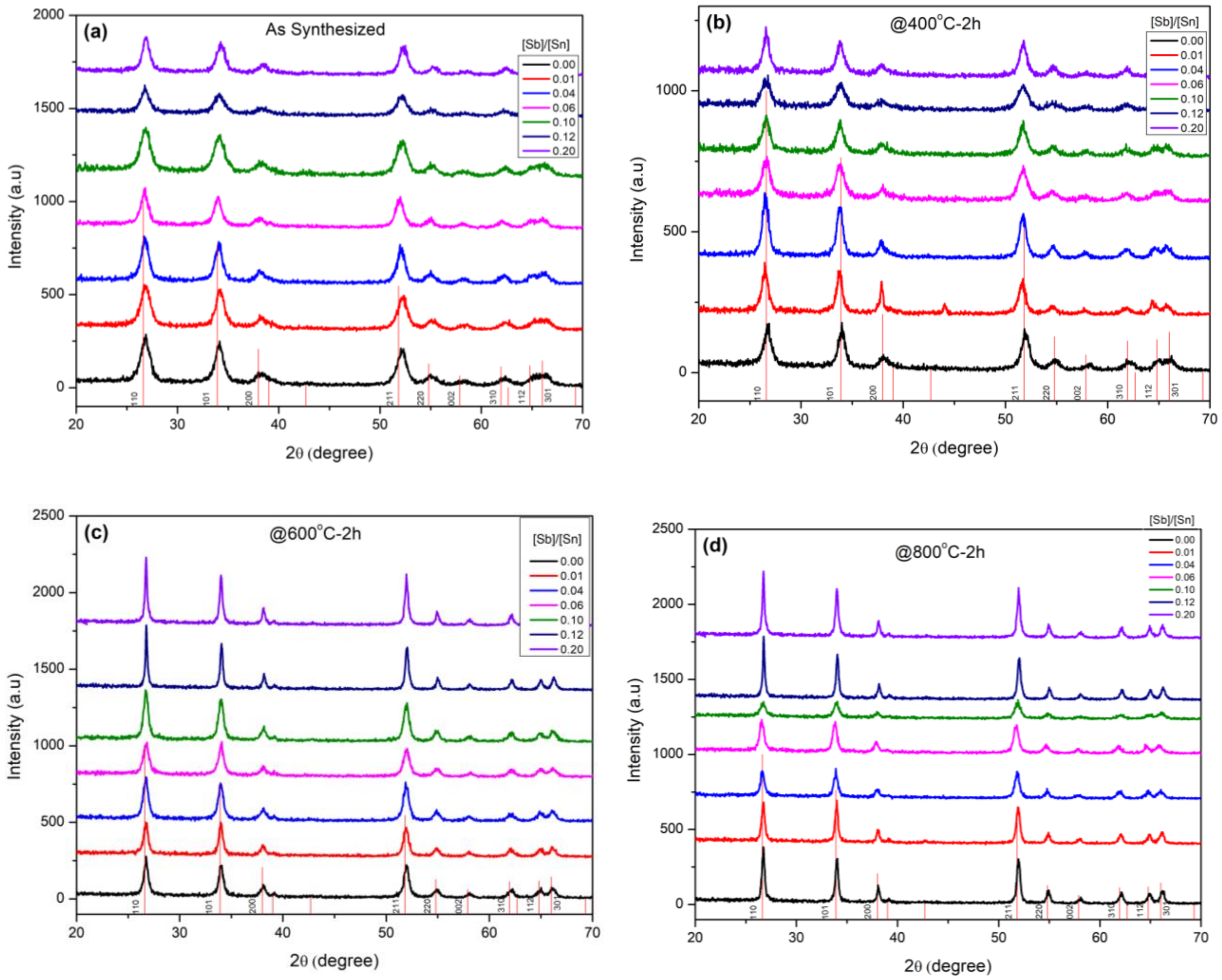

Figure 3.5. XRD results of ATO samples (a) as-synthesized samples. (b) post-annealed samples at 400℃. (c) post-annealed samples at 600 ℃. (d) post-annealed samples at 800 ℃. The red lines at the bottom correspond to tetragonal SnO_2 reference peaks (JCPDS 88-0287).

from Scherrer equation in Figure 3.6 show a reasonable correlation with the TEM results by predicting a mean crystallite's size of about 10.10 and 10.03 nm for SnO_2 and ATO-12 respectively. It was stated earlier in this thesis in Section 1.3 that Sb^{3+} ions display a larger ionic radius than Sn^{4+}; whereas Sb^{5+} exhibits a smaller ionic radius. The incorporation of these two ions can lead to an overall increase or decrease of the unit cell size and subsequently a shift in the position of the diffracted peak. Determining the XRD peak position can help in determining the oxidation state of incorporated antimony atoms. Whereas, Scherrer equation can help understanding the rule of dopant ions in inhibiting or promoting the NC growth. The NCs appear to be larger at antimony doping concentration of 6 % as presented in Figure 3.6. Herein, it is relevant to add that the parabolic shape of the size trend is consistent with the expected behavior for ATO NCs according to Zhang and Gao (2004).[59]

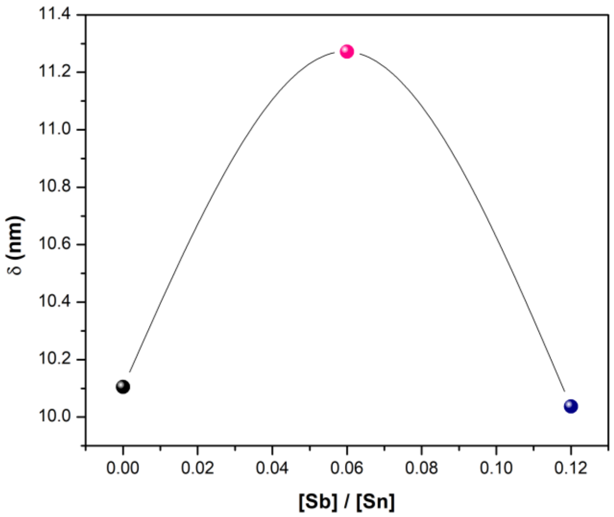

Figure 3.6. Crystallite size trend of SnO_2 and ATO-6 and ATO-12 calculated from Scherrer's equation. The size was calculated based on (110) reflection. The solid line is a guide for the viewer's eye.

It is hypothesized in this study that thermal treatment will force some aggregated antimony atoms to leave the grain boundaries and move to the surface. If this is correct, then a generally crowded surface is expected to form which will likely have a crucial rule in the photocatalytic study. In addition, literature work on SnO_2 has demonstrated that annealing the samples at an elevated temperature in air will generally remove oxygen vacancies by incorporating more oxygen atoms into the lattice.[73] This means that oxygen vacancies are less likely to contribute to the LSPR mode of the annealed samples in this study.

3.2. Optical study of SnO_2 and ATO

3.2.1 Detection of LSPR presence through UV-MIR absorption

Optical absorption measurements were performed on all ATO samples to detemine their band gap and confirm their LSPR feature. In this study, colloidal samples were deposited on a quartz slide and left to naturally dry, forming a thin film as explained in the experimental section. Depicted in Figure 3.7 (a) the UV-MIR spectra for SnO_2 and ATO-12. Figure 3.7 (b) shows the deduced band gap energies from Tauc plot for all as-synthesized smaples. The UV-MIR result indicate the existence of the LSPR property in ATO-12 NPs. The absorption starts in the NIR region around 1170 nm and continues toward MIR. A full picture cannot be drawn before studying the rest of the absorption peak using FTIR spectroscopy.

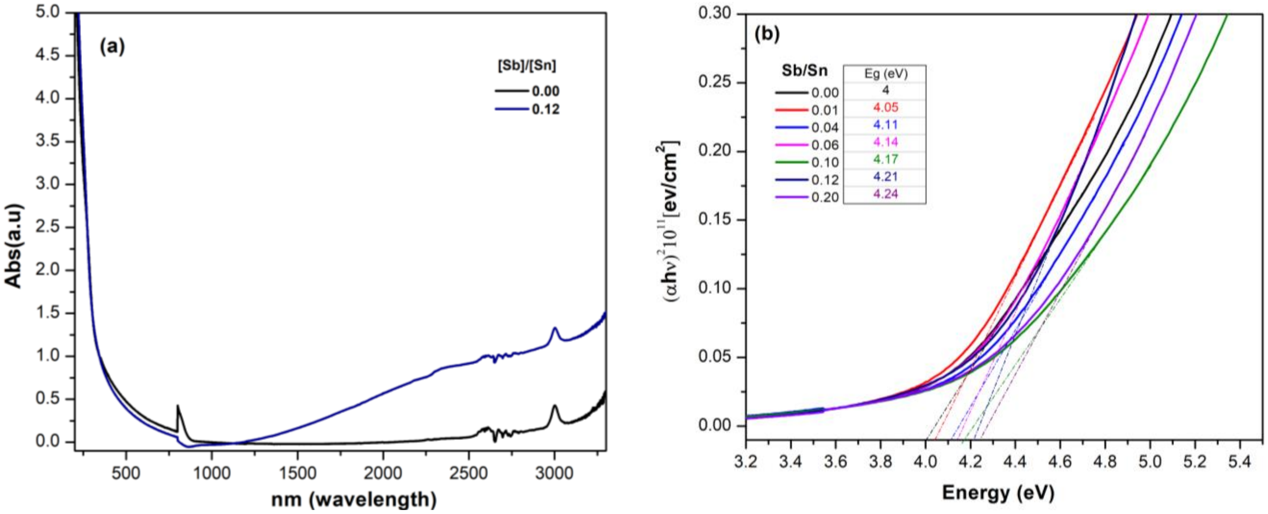

Figure 3.7. (a) UV-MIR results for as-synthesized SnO_2 and ATO-12 normalized to the band gap. (b) Tauc plot of as-synthesized samples.

As for the Tauc plot, one of the major indications of the data is the enhanced carrier concentration in the CB upon increasing the dopant concentration. Hence, a reasonable conclusion to make is that more tin atoms have been effectively replaced by antimony atoms, which effectivly influnced the optical band gap energy.

3.2.2 Exploiting the LSPR feature from FTIR spectra

The results from UV-MIR of SnO_2 and ATO-12 were merged with the normalized IR spectra to present the complete feature of LSPR peaks. Details on merging steps are found in the thesis work of Hanbing Fang.[74, 75] As can be seen in Figure 3.8, the plasmon peak for ATO-12 exists in MIR and NIR. The absorption band around 2872 nm is characteristic for OH stretching mode.[36] Unlike the LSPR feature that persists in MIR for ATO-12, the assigned OH peak readily vanishes around 3835 nm indicating the absence of the LSPR property in pure SnO_2.

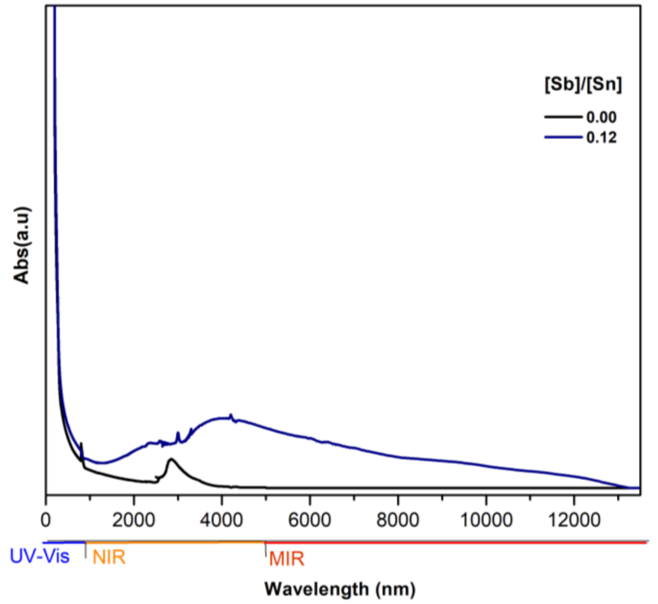

Figure 3.8. Representation of ATO-12 LSPR peak in the IR region. The color code below the bottom axis indicates the electromagnetic wave that corresponds to each wavelength's range, MIR; red, NIR; orange; UV-Vis; blue.

In the current study, the samples were mounted between two KCl solid plates and scanned with an FTIR insturment in the transmission mode. The scattering of the transmitted light created large insturmental errors and prevented accurate comparison between different results. Therefore, the carrier density was only determined for ATO-12.

As stated in Section 1.1.1, the carrier concentration corresponds to the frequecy of the highest absorption intensity of the plasmonic peak. The carrier consentration of ATO-12 was caculated using Equation 1.1. in the first Chapter and was found to be 6.13×10^{20} cm^{-3}.

3.3. Photoemission study of SnO_2 and ATO

3.3.1. Analysis of SnO_2 and ATO oxidation states via XPS

XPS was perfomed on a couple of pelletized ATO samples to extrapolate their oxidation states and correlate that with the thus far obtained results. The data was first charge corrected to adventitious C 1s displayed in Figure 3.9 (a). The C peak was deconvoluted to different carbon species with the alpha peak of alcohol and ether bonding being positioned at 284.5 eV for all samples. The peak that corresponds to Sb $3d_{5/2}$ overlaps with O 1s photoemission peak, and seems to grow stronger in intensity with increasing annealing temperature. The red rectangle highlights the observed trend. The trend can be ascribed to the decrease in oxygen vacancies and the increase in oxygen content in lattice sites or as adsorbates at the surface.[76]

Table.3.1 Extracted Sn and Sb(V) concentrations from XPS spectrum

[Sb]/[Sn] nominal concentration (mol%)	Treatment condition	Real [Sb]/[Sn] from XPS (mol%)	Molar fraction of Sb^{5+} (mol%)
0.06	As-synthesized	0.04	75.21
0.06	Annealed at 600 ℃	0.09	53.33
0.06	Annealed at 800 ℃	0.19	10.09
0.12	As synthesized	0.07	81.60
0.12	Annealed at 600 ℃	0.18	94.57
0.12	Annealed at 800 ℃	0.26	100.00

It is clear from Figure 3.9 (b) that no froreign atoms were detected in the survey sepctra. The binding energy of Sn $3d_{5/2}$ in example (c) corresponds to the oxidation state for Sn^{4+} whereas the distance between Sn $3d_{5/2}$ and $3d_{3/2}$ accounts for O and Sn species in SnO_2 lattice.[77] Gaussian deconvolution of Sb $3d_{3/2}$ peaks around 540 eV allowed for the determination of Sb^{3+} and Sb^{5+} ratio in the studied samples.[38] Quantification of Sn and antimony component was achieved by dividing the ratio of Sb $3d_{3/2}$ by Sn $3d_{3/2}$ using Scofield sensitivity factor.[72] As seen from Table 3.1, the as-synthesized samples greatly suffer from surface enrichment with increasing annealing temperature. The signal to noise ratio of antimony peak grows sharper upon annealing, indicating that a particular specimen is becoming more dominant.[76]. Hence, the data suggest that annealing at elevated temperatures forces antimony atoms to leave either their lattice interstitial or substitutional sites and move to the surface. The data does not confirm the origion of surface antimony but in principle, diffused antimony atoms can oxidize the surface and create more Sb^{5+}. The deconvoluted Sb $3d_{3/2}$ peak area was used to infer the concentrationof Sb^{5+}.[38]

In the case of ATO-12, more Sb^{5+} was detected on the surface, regardless of the treatment condition, indicating a plausibly higher carrier density in the CB. Nevertheless, there is no clear explanation for the origion of the higher antimony content in the annealed samples that exceeded the starting concentration.

In the contrary, ATO-6 samples show a clear tendency to accommodate Sb^{3+} atoms at the surface. Diffused Sb^{3+} atoms from the bulk to the surface are expected to lower the CB density and increase the density of holes in the VB. Finally, it is relevant to indicate that the observed

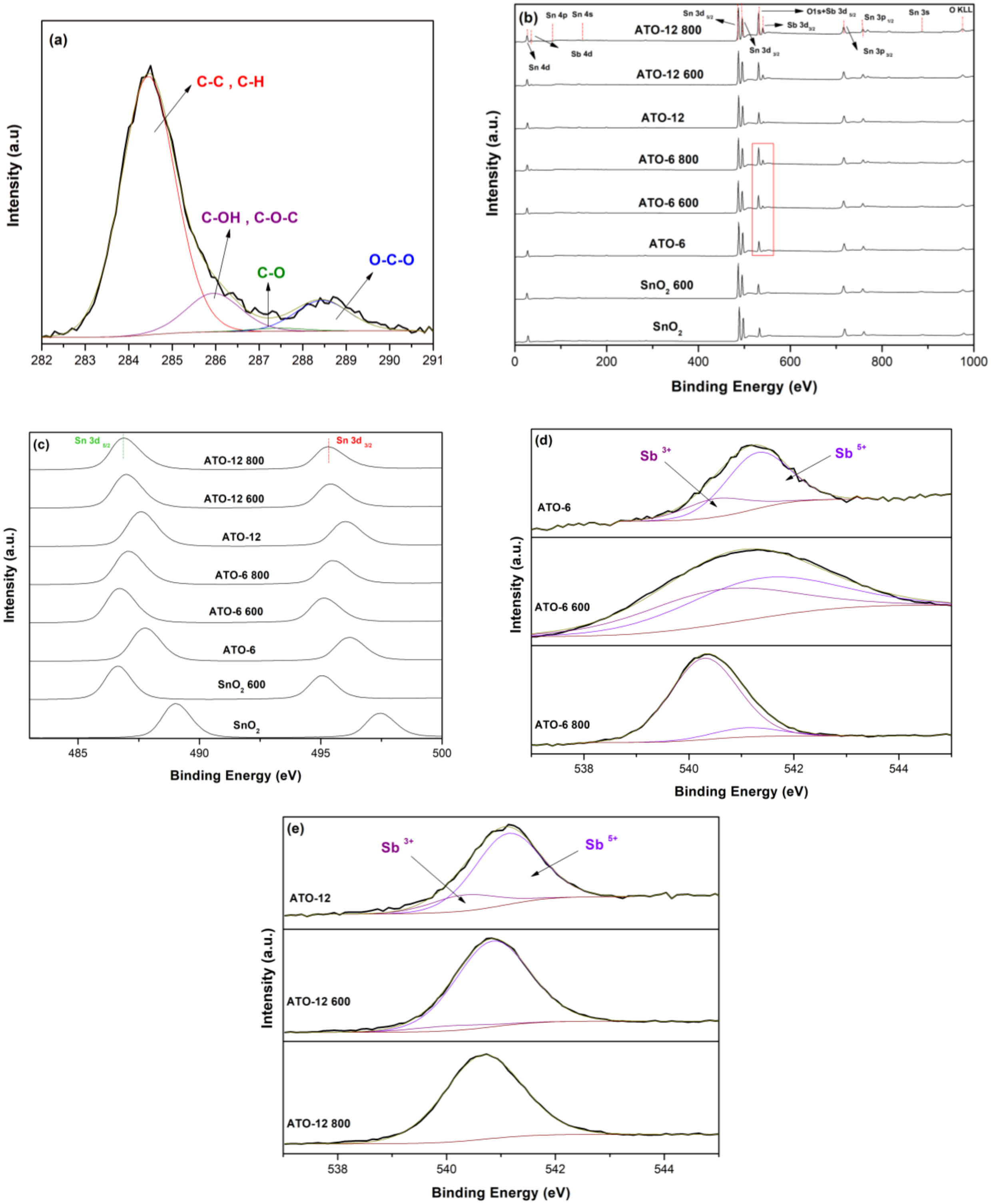

Figure 3.9. Display of XPS results (a) adventitious C 1s model peak used for charge correction at 284.5 eV. (b) Full XPS spectrum of scanned samples. (c) High resolution Sn $3d_{3/2}$ and $3d_{5/2}$ profiles. The rectangle focuses on the area of $Sb_{5/2}$ and O 1s overlapping peak where

the satellite peak grows stronger in intensity (d) Gaussian deconvolution of high resolution Sb $3d_{3/2}$ peak for ATO-6 samples and (e) ATO-12 samples.

surface enrichment will plausibly influence any surfaec related properties such as the adsorption of dye molecules in photocatalysis, and thus must be accounted for in the upcoming studies.

Chapter 4

Studies of ATO's Plasmonic Photocatalysis

4.1. Understanding the photocatalytic performance of ATO in the dark

Prior to studying any plasmonic relatd photocatalysis, it is important to clarify the procedure of the organic molecules degradation process. According to the reported energy level of of SnO_2, the CB lies 0.2 eV below the NHE oxidation potential at pH=0.[78] This can prevent the utilization of electron species in dye degradation. Thus, the degradation process will only occur if the electron concentration is high enough to fill up the empty levels until above the oxidation potential. The degradation may also occur through another senario where the CB electrons get excited to a point above the oxidation potential using IR-thermal emission. From Equation 1.18 in Chapter 1, the maximum thermal emissive power at RT corresponds to an energy value of 2.82×10^{-6} eV. Apparently this energy is far lower from being enough to excite the electrons in SnO_2 VB to a point above the oxidation potential. Thus, the degradation *via* thermal excitation is only possible if the electron concentration is higher than the oxidation potential, which is hoped to be achieved *via* doping SnO_2 NPs with antimony atoms.

In this project, the study of thermal-IR photocatalysis presents the challenge of differentiating between adsorption and dye degradation. In a typical study, the first step will include leaving the sample to stir in the dark for a given amount of time before irradiating the reaction mixtuer. In the present study however, both the adsorption and degradation *via* expousure to thermal-IR radiation will happen concurrently in the dark at RT. This brings in the importance of establishing a control experiment that can distinguish the adsorption from other plasmonic related activities. To do so, pure SnO_2 was selected as a reference sample for adsorption since it is mostly a plasmon-free sample and thus is not expected to show any thermal-IR response.

4.1.1. *Verifying the validity of SnO_2 as an adsorption reference*

To verify that SnO_2 is a proper reference for studying adsorption, the photocatalytic study was first performed on as-synthesized and post-annealed SnO_2 samples. A common belief exists that defect formation in SnO_2 crystal lattice is almost inevitable since SnO_2 tends to adopt some natural lattice defects, such as oxygen vacancies, during the growth stage.[1, 37] Accommodated oxygen vacancies are known to donate electrons to the CB and enhance the overall conductivity of the material.[79] Therefore, the samples in this study were annealed at elevated temperatures to eliminate the effect of oxygen vacancies.

Figure 4.1 shows that all SnO_2 samples exhibit a very low photocatalytic activity in the dark. The obtained results from annealed SnO_2 are vital in confirming the argument that the removal of dye molecules from the solution is solely due to adsorption on NC surface regardless of the presence of some CB electrons created by oxygen vaccancies. As can be seen, the activity is similar for all samples and the difference lies within the error range. In addition, XRD results showed that annealed SnO_2 samples exhibit a larger crystallite size which means they display a

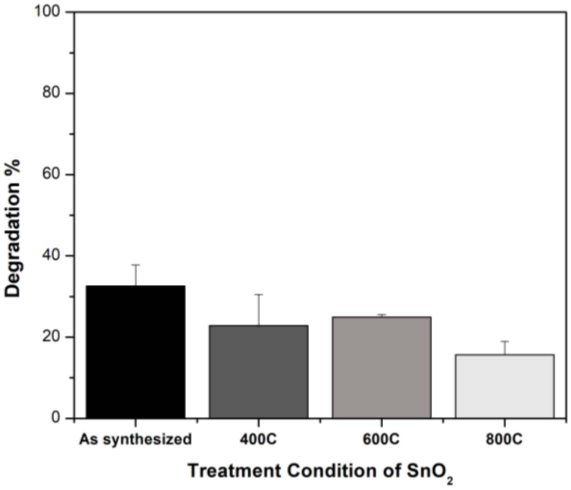

Figure 4.1. Demonstration of the photocatalytic activity of as-synthesized and post-annealed SnO_2 samples in the dark

somewhat smaller surface area than non-annealed SnO_2 (Table B.1). This clearly explains the reason behind the slightly better activity of non-annealed SnO_2, though it is important to state that the differnce in the activity is still withen an error range. So, it is accurate to solely attribute all of the so far observed decrease in dye concentration to adsorption in spite of the treatment condition. Based on this, SnO_2 activity will be used as a reference to distinguish adsorption from degradation related activity in the ATO photocatalytic study.

When it comes to the rest of the as-synthesized samples, the samples from SnO_2 to ATO-6 display similar activity as illustrated in Figure 4.2. It is assumed here that Rh-B will get attached to SnO_2 and ATO NPs through the surface and grain boundaries. In that sense, introducing the dopant atoms will reduce the number of available active sites due to the fact that antimony atoms tend to aggregate at grain boundaries. As a consequence, the adsorption of ATO samples will be smaller relative to pure SnO_2, and the decrease will be most pronounced at high dopant levels starting from ATO-10. Another factor that can also be responsible for the lower adsorption of highly doped samples is the presence of Sb^{3+} oxidation state. As has been stated earlier in this

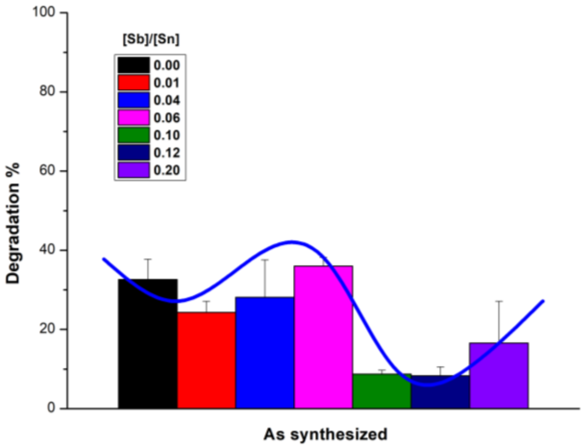

Figure 4.2. Demonstration of adsorption trend of as-synthesized samples.

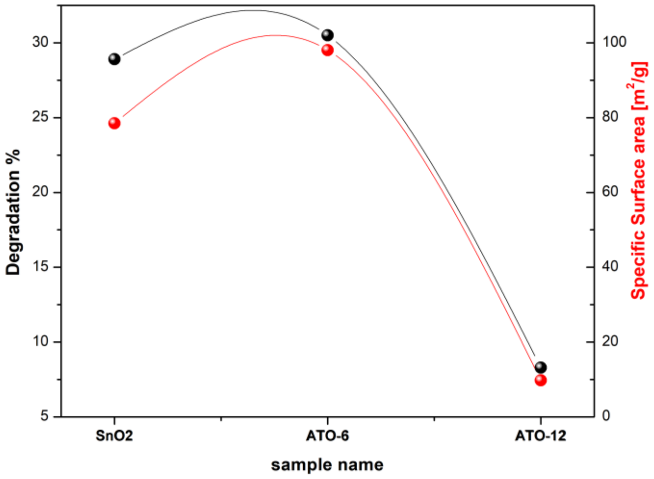

Figure 4.3. Demonstration of degradation percentage combined with the specific surface area of SnO_2, ATO-6 and ATO-12. The solid lines are guide to the eye and their color corresponds to the color of the side axes.

thesis, highly doped ATO NPs host both Sb^{5+} and Sb^{3+} at high dopant concentrations, and Sb^{3+} leads to larger crystallite size, and herin, a smaller surface area. That is to say, adsorption on the highly doped samples was affected by two main factors; the blockage of active sites by aggregated antimony atoms and the smaller surface area of the larger crystallites when Sb^{3+} got incorporated into the lattice.

To further confirm the origin of the samples activity, the surface area measurements were performed on three different samples at 77 K. From the BET results in Figure 4.3, one can see that the adsorption is consistent with the trend of the surface area; especially, the large drop of ATO-12 surface area that coincides with the drop in the adsorption percentage. Based on current observations, it is safe to ascribe the reduced dye concentration of as-synthesized ATO, non-annealed and post-annealed SnO_2 samples to adsorption. In addition, thus far, the LSPR mode in the as-synthesized samples is not showing any respectful contribution; possibly because the CB electron density doesn’t fulfill the requirement for the degradation process to occur or just simply because the dye molecules couldn’t successfully attach to the surface. Therefore, the study was resumed after annealing the samples at a temperature of 400, 600 and 800 ℃ for 2 hours.

4.1.2. *Unraveling the role of annealing and antimony concentrationin the photocatalytic activity*

Some of ATO post-annelaed samples, presented in Figure 4.4, started to show an appreciable amount of activity in the dark. This activity is primarily attributed to LSPR reponse to RT thermal activation. As has been outlined in Section 4.1.1, the samples’ adsorption is based on SnO_2 activity under each treatment condition. From Figure 4.4 (a) to (c), the annealed ATO samples either show a comparable or higher activity than annealed SnO_2 which can be a positive sign. In principle, the photocatalytic activity is expected to show a gradual enhancement from ATO-1 up to ATO-12, and then the activity might decrease toward ATO-20. This perception is based on the band gap results where the CB electron density increases from ATO-1 to ATO-12 resulting in higher energy values (Figure A.1). By following the direction of the virtual trend, a decrease in the band gap energy is expected to occur at some point before reaching 20% doping concentration. The best match between the band gap and degradation trend is available for post-annealed ATO 600 samples. Thus, it might be too soon to relate the decrease in dye concentration for ATO 400 and ATO 800 samples to LSPR activity, and it is still important to compare the photocatalytic

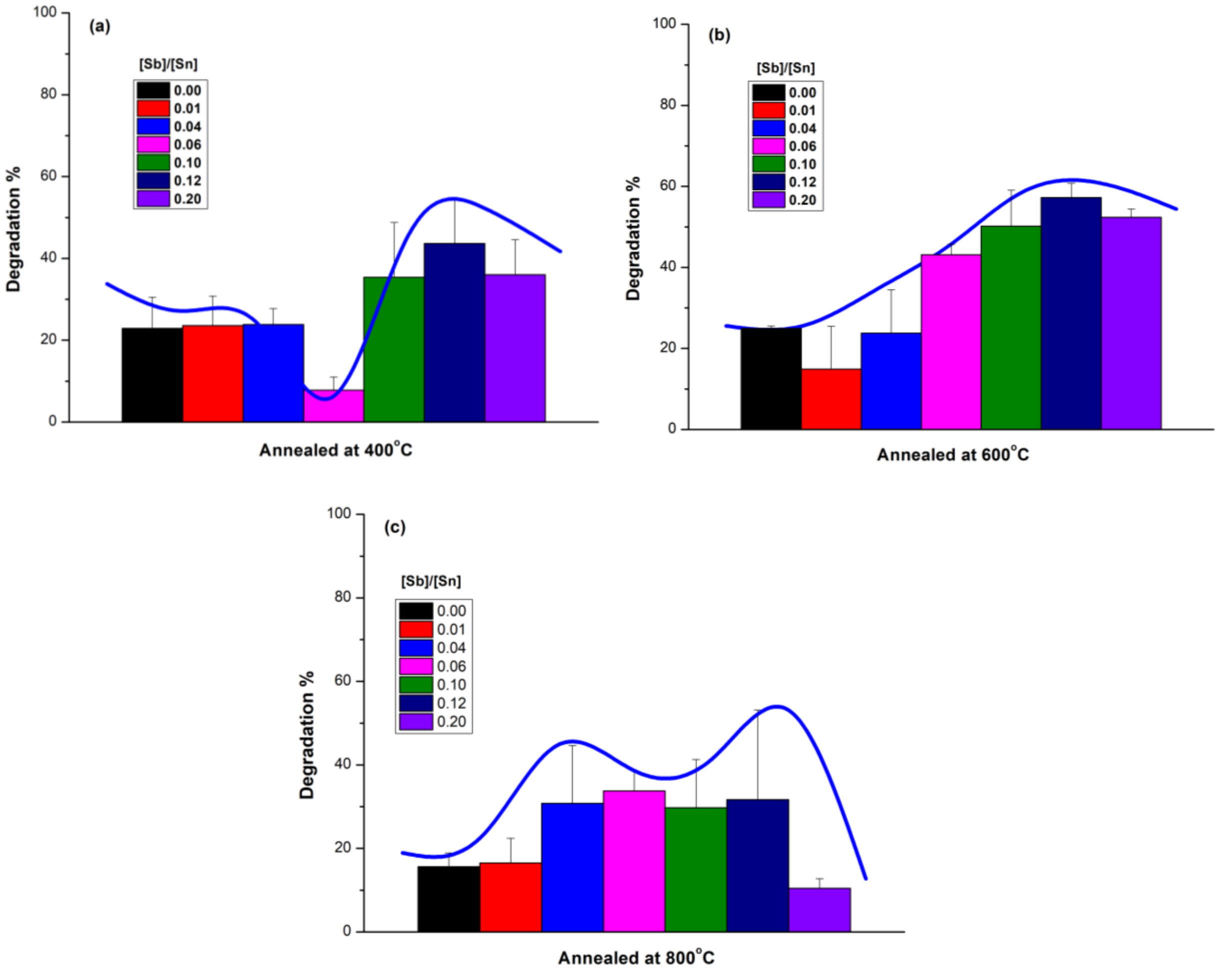

Figure 4.4. Analogy study of the photocatalytic activity of ATO samples annealed at (a) 400 °C. (b) 600 °C. (c) 800 °C. The solid blue lines demonstrate the activity trend.

activity of these samples against their as-synthesized counterparts. Also, it is worth mentioning that highly doped ATO 600 samples exhibit a larger grain size than their as-synthesized counterparts, theoretically due to thermal expansion or fusion of NCs. Scherrer equation also predicts a larger crystallite size for annealed NPs. This means the samples should display a smaller surface area, and yet the photocatalytic activity scales higher than the non-annealed samples. This observation confirms that the enhanced photocatalytic activity for ATO 600 samples in specific is not adsorption related and is mostly assigned to LSPR feature. Nevertheless, not all ATO annealed samples at 400 ℃ and 800 ℃ are performing a good dye degradation activity and the reason behind that is still ambiguous at this point.

In order to address the low activity of certain post-annealed ATO samples, the results were plotted in a different way with respect to each samples' activity trend. The results were seperated into two groups; the first group corresponds to the low dopant concentrations from 1 to 6%, and the second is the highly doped samples from 10 to 20%. It is worth mentioning that the latter group shows a good match in their trends under different treatment conditions.

First, multiple work on annealed ATO NPs have demonstrated that annealing ATO powder and thin films at an elevated temperature removes some of the oxygen vacancies, increases grain size, shrinks grain boundaries and increases surface roughness.[58, 79, 80, 81] The shrink of grain boundaries forces some aggregated antimony atoms to move from the boundaries to the surface. In addition, annealing also triggers the diffusion from the bulk to the surface which increases the surface roughness. The latter case is related to the availability of lattice sites for the atoms to occupy. Some interstitial antimony atoms will replace tin atoms in their vaccancy V_{Sb} or substitutional sites and donate the extra electrons to the CB to conserve charge neutrality. Excessive antimony atoms that could not occupy a proper lattice site will diffuse to the surface. The current results cannot reliably assign diffused antimony atoms to the substitutional or interstitial sites; thought, the diffusion is confirmed from the XPS results where more antimony atoms have been detected on the surface after anneling.

Annealing the smaples at 400 ℃ will affect the CB density in such a way that CB electrons originated from oxygen vaccancies will be decreased or eliminated. It can be suggested that either the potential of ATO-1 400 to ATO-6 400 is not sufficient to fill up the empty CB levels in order

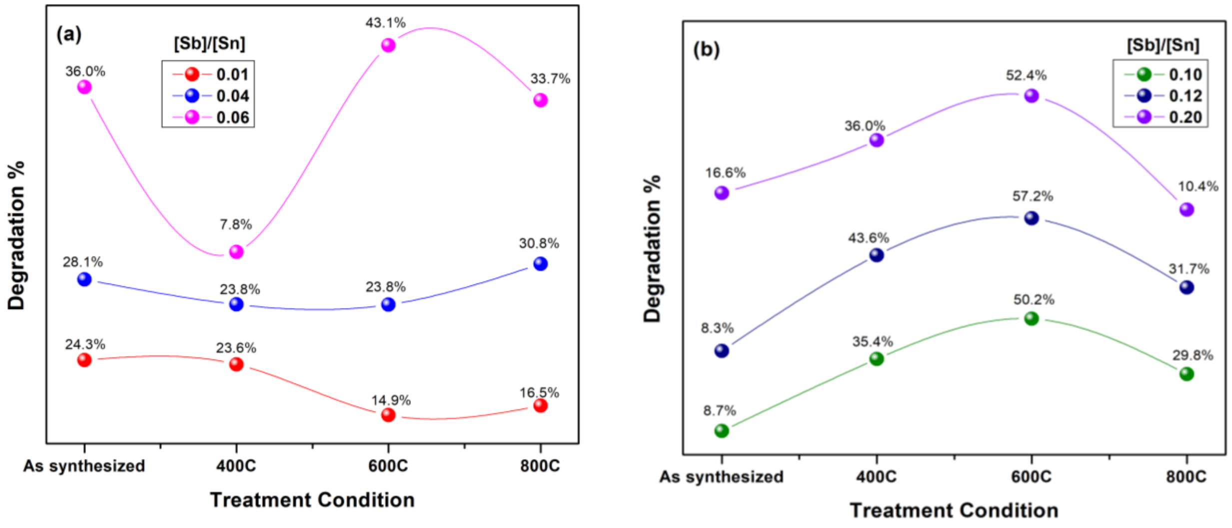

Figure 4.5. Display of ATO photocatalytic activity trends under each treatment condition. (a) Low dopant concentrations. (b) Highly doped samples

to match the NHE oxidation potential or the CB potential is possibly too high for the oxidation reaction to occur. As a result, the corresponding samples exhibit a similar activity to their as-synthesized counterparts, which suggests that any change in dye concentration is assigned to adsorption.

ATO 400 highly doped samples on the other hand, show a noticable increase in their activity after annealing. This can be attributed to the removal of aggregated antimony atoms at grain boundaries which cleared the path for the dye molecules to adsorb at active sites in grain boundaries. Concurrently, some antimony atoms are expected to leave the grain boundaries and block the active sites at the surface. The reduction in the number of active sites at the surface is overbalanced by the availability of more active sites at grain boundaries which allowed for effective attachement between dye molecules and catalyst NPs. The dye concentration in that case goes down and is relatively higher than that of SnO_2 400, which suggests that the observed decrease in dye concentration is degradation related.

The continuous increase of the annealing temperature is expected to lead to more reduction of the grain boundaries and more antimony atoms will be expelled from both the boundaries and the substitutional or interstitial sites and forced to move to the surface. As a result, all highly doped ATO 600 samples along with ATO-6 600 show a better photocatalytic performance with respect to SnO_2 600 and their as-synthesized counterparts. It is relevant to mention that more proof is needed to support this assumption. As for 600 ℃ annealed ATO-1 and ATO-4 they exhibit an activity that is either similar or lower than the as-synthesized counterparts. Hence, the most plausible explanation for the decreased dye concentration is adsorption.

When the annealing temperature reaches 800 ℃, the photocatalytic activity for the samples from 6 to 20% dopant concentration seems to decrease. The XPS results of ATO-12 800 excludes the likelyhood of Sb^{5+} getting reduced to Sb^{3+} and consuming some of the CB electrons. So, a different key factor must be responsible for the lower activity.

Korber et. al, mentioned in their paper that exposure to highly oxidizing environment can lead the oxygen molecules to adsorb at grain boundaries and act as trapping centers for CB electrons.[76] Moreover, the stoichiometric system of ATO-800 samples will accommodate a certain percentage of antimony atoms and the excessive atoms that could not occupy proper lattice sites will be expelled to the surface. Ionized antimony atoms and adsorbed oxygen molecules reduce the number of active sites at the surface and hindere dye adsorption. Thus, the first factor is related to the reduction of active sites due to ionized impurities and electron trapping.

The second contributing factor for the lower activity may be caused by improved crystallite size. Larger crystallite size is generally accompanied by a smaller surface area and lesser active sites. As a result, there is less active sites for the dye molecules to adsorp.

The activity doesn't change much for ATO-1 800 and ATO-4 800 and the small increase in ATO-4 800 activity is assigned again to active sites availability. So, for all ATO 800 samples, the decrease in dye concentration is ascribed to adsorption.

As a confirmation of the assigned activities at different treatment conditions, ATO-6 400 was selected as a representative for photocatalytically non-active samples and ATO-12 600 was the representative for active photocatalysts. The inverse correlation between ATO-12 600 degradation activity and specific surface area in Figure 4.6 confirms that the origion of ATO-12 600 activity is not adsorption related. Adding to that, pure SnO_2 and ATO-6 400 display a higher surface area and yet their photocataltic performance scales lower than ATO-12 600. In other words, the trend for ATO-6 400 is more consistent with SnO_2 and a positive correlation exists between the two samples' activity and surface area. Therefore, it is correct to ascribe ATO-6 400 activity to adsorption only.

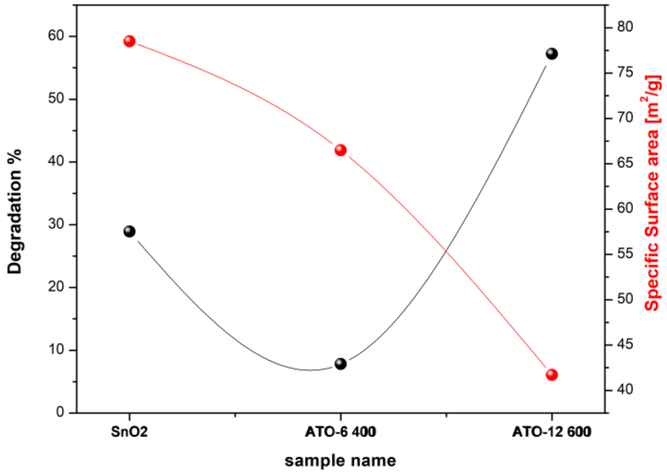

Figure 4.6. Demonstration of degradation percentage combined with the specific surface area of SnO_2, ATO-6 600 and ATO-12 600. The solid lines are guide to the eye and their colors correspond to the color of the studied parameter.

Thus far, based on the aforementioned analysis, the only samples that are photocatalytically active and were able to respond to thermal-IR excitation are ATO-6-600, ATO-10 400, ATO-10 600, ATO-12 400, ATO-12 600, ATO-20 400 and ATO-20 600. It is important to mention that these results do not contradict the fact that all the doped samples have a contribution from Sb^{5+} in their CB electron density based on their band gap values, FTIR and visual color. This means the LSPR mode of these samples can be thermally activated at RT. However, the results underline the fundamental role of engineering the CB to match water oxidation potential and cleaning the surface to avoid electron trapping in order to perform the degradation reaction.

In order to track the improvement in the degradation by the seven active samples, their degrdation percentage was substracted from the adsorption percentage of their as-synthesized counterparts. The results are listed in Table 5.1. So, according to Table 5.1, the efficiency of the photocatalytic activity will gradually improve with increasing dopant concentration and will finally drop after reaching the optimum dopant level before 20%.

Table.4.1 Tabulated comparison of the plasmonic photocatalytic activity of different ATO samples

Sample Name	Annealing Temperature	Efficiency Improvement	Annealing Temperature	Efficiency Improvement
ATO-6			600	7.1 %
ATO-10	400	26.6 %	600	41.4 %
ATO-12	400	35.3 %	600	48.9 %
ATO-20	400	19.4 %	600	35.8 %

To sum up, the availability of active sites at the surface and grain boundaries is the key factor for dye adsorption. Annealing the samples at a high temperature is a fundamental step to clear the path for adsorping dye molecules at grain boundaries. XPS data suggest that more antimony atoms are present at the surface at higher annealing temperatures which reduces the number of active surface sites and, susequentally, adsorbed dye molecules. Annealing at 600 ℃ provided the best condition where the effect of oxygen depletion layer is negligible and enough active sites are availble at the surface and grain boundaries. Although the LSPR oscilative mode can be activated at RT, the degradation reaction will not occur unless the CB surpasses the NHE oxidation potential. So, the higher dopant concentration along with the higher annealing temperature serve in allowing the oxidation potential to reach the optimum condition for the degradation reaction to occur.

4.1.3. Correlating medium temperature with thermal-IR photocatalysis

It was stated in Section 1.5 that thermal emission can work as an IR radiation source because the amount of emitted energy matches that of IR radiation at certain wavelengths. To put this concept to test, the samples were exposed to different temperatures *via* heating or cooling the experimental solution prior to the conducted photocatalytic experiment. Also, in order to preserve the temperature at a certain degree throughout the experiment, a water jacket was used and was connected to a circulating bath until the end of each experiment. Since the used medium in these studies is water, it was necessary to avoid freezing or boiling the water molecules; therfore, 1 ℃ and 45 ℃ were selected as the medium temperatures. Also, ATO-12 was chosen to be the model sample since it had a high electron density from band gap energy and showed the best photocatalytic performance after being annealed at 600 ℃. SnO_2 and ATO-6 800 were selcted as controls.

The results in Figure 4.7 (a) clearly indicate that SnO_2 and ATO-6 800 have no clear photocatalytic response toward thermal-IR excitation. The photocatalytic activity of ATO-12

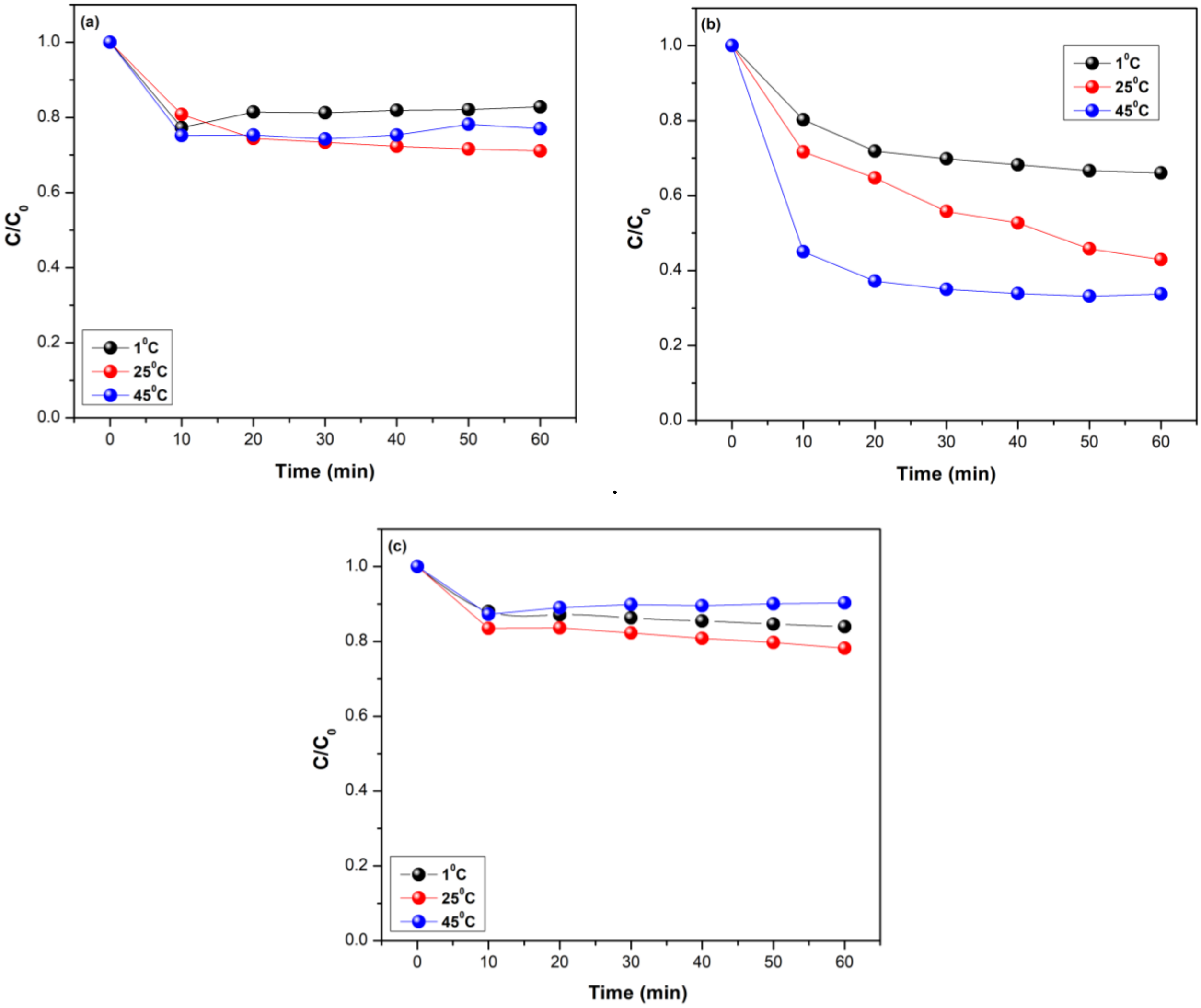

Figure 4.7. Thermal Photocatalytic Study of (a) SnO_2. (b) ATO-12 600. (c) ATO-6 800.

600, on the other hand, takes a clear path of increasing degradation rate with increasing the medium temperature. The later result supports the argument that the previously registered photocatalytic activity from the seven different post-annealed samples is a response to thermal-IR excitation at RT.

4.1.4. Exploiting the response of SnO_2 and ATO to UV combined with thermal -IR excitation

Performing the photocatalytic study of pure and doped SnO_2 samples under UV illumination can reveal some information about the interaction of LSPR electrons and photogenerated free carriers. Thus, the photocatalytic experiments were also performed by stirring the samples for 60 minutes in the dark and then shining two 40W UV lamps on the reaction medium. The degradation rate was determined using Equation 2.4 in Chapter 2 assuming a first order degradation mechnism, and C_0 was set to be the dye concentration after 60 minutes of stirring in the dark. Although pure SnO_2 is known to be photocatalytically active under UV excitation; the results displayed in Figure 4.8 suggest that this semiconductor's activity was hindered by doping and annealing. First, annealing can induce a thermal expansion of the crystallite size which reduces the number of surface sites. As a consequence, the adsorption amount of the dye molecules gets reduced. In addition, annealing aslo removes some of the natural defects in the lattice such as oxygen vaccancies. Oxygen vaccancies create new energy levels inside the band gap which act as defect centers that can capture the photogenerated electrons.[43] This can influnce the degradation activity of the catalyst by prolonging the life-time of photogenerated electrons. In that sense,

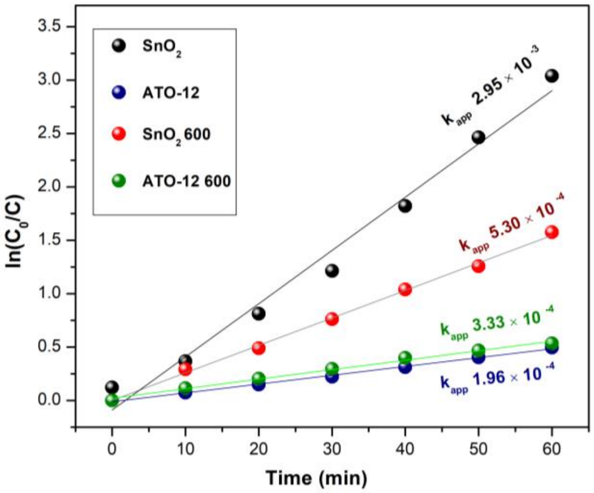

Figure 4.8. Illustration of UV photocatalytic activity combined with thermal-IR response of SnO_2, ATO-12, SnO_2 600 and ATO-12 600.

annealed SnO_2 has less defects than non-annealed SnO_2. As a results, SnO_2 600 shows a lower degreadtion activity than its as-synthesized counterpart due to the higher recombination rate of free carriers.

Another factor that comes into play is doping the sample with foregion atoms that can aggregate at grain boundaries and prevent the dye molecules from effectively reaching the active sites. The aforementioned surface area in Figure 4.3 have shown that ATO-12 displays a smaller surface area than SnO_2 which leads to a smaller adsorption.

Lastly, the LSPR electrons in ATO-12 600 are plausibly undergoing high scattering events with photoinduced free carriers. So, despite the fact that the dye molecules have a better potential of reaching the surface sites of annealed ATO samples, there is still the scattering effect and the blockage of a portion of active sites by surface migrated antimony atoms. So, generally speaking, ATO samples are less competitive than pure SnO_2 under UV illumination. Nonetheless, the photocatalytic activity of ATO-12 seems to have slightly improved after annealing the samples.

To sum up, the effeciency of SnO_2 photocatalytic activity under UV light is significantly reduced by annealing or doping. In addition, thermally activated LSPR electrons show a negative effect on the degradation rate when an additional excitation source is applied. So, unlike the LSPR samples that are beneficial for IR photocatalysis, non-treated SnO_2 is by far the best candidate for UV photocatalysis.

Chapter 5

Determination of Rh-B Degradation Mechanism Using Sacrificial Reagents

5.1. Trapping experiments' procedure

The determination of the degradation process is an important step of any photocatalytic study. Usually, the trapping experiments are performed to extract information about the reaction path, the limiting step and the most active species in the reaction. In the case of SnO_2 NPs, holes and $^{\bullet}OH$ radicals are the most frequently reported species to be active in organic dye degradation.[78, 82, 83] Some literature work have reported CH_3OH (MeOH), $AgNO_3$ and isopropanol (Iso.pro) as active hole, electron and $^{\bullet}OH$ scavengers respectively. Therefore, the three reagents have been employed in the current study.[84, 85, 86, 67]

The experiments were performed by a simultaneous addition of the studied catalysts with 30 mM of MeOH or 3 mM of $AgNO_3$ or isopropanol to the reaction medium. To insure the accuracy of the results, each trapping experiment was repeated three times. In addition, the sample selection included inactive SnO_2 and ATO6 800 for control experiments. Finally, the study also included reflecting a UV light on the experimental medium to study the impact of the scavengers when two excitation sources are present.

5.2. Study of plasmonic photocatalysis in the presence of sacrificial reagents

As Figure 5.1 illustrates, the electron scavenger, $AgNO_3$, only impacts ATO-12 600 sample and reduces the degradation average from 57 to 3%. This result is an additional proof that ATO-12 600 photocatalytic activity is related to LSPR activity in which CB electrons start a faster monotonic oscillation after being exposed to thermal excitation.

In the case of MeOH, all samples seem to show a similar activity when the scavenger is absent. The variation in ATO-12 600 activity can be attributed to the competion between MeOH and dye molecules to occupy the surface sites of the catalyst. Due to the fact that the involvement of the electrons in the degradation can be indirect through intermediate products, isopropanol was also used to test the presence of $^{\bullet}$OH radicals.

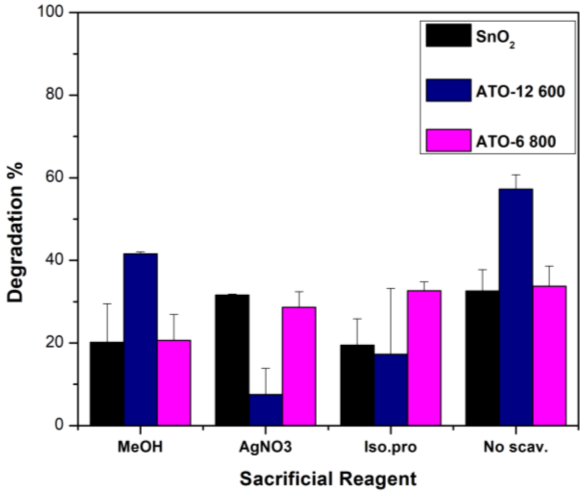

Figure 5.1. Results from trapping experiments using MeOH as a hole, $AgNO_3$ as an electron and isopropanol as OH radical scavenger. The results are compared against those with no scavenger (No scav.) addition.

The observable decrease in ATO-12 600 activity suggests that Rh-B degradation involves several steps in which intermediate products are obtained. Hence, one of the limiting steps is when $^{\bullet}$OH radicals are created, and the use of a hydroxyl scavenger can hinder the degradation reaction to a certain extent. The scenario involving $^{\bullet}$OH radicals that are generated from electron species involvement has been reported in a number of literature work.[78, 83, 87]

It is useful to mention that there is a striking resemblance in the way ATO-12 600 responded to the presence of an electron scavenger and all of the other 6 active samples in Table 5.1 (Figure C.1). Such results confirm the accuracy of the assigned activities in Figure 4.5.

The proposed pathway of the degradation mechanism is summarized in Figure 5.2 (a) to (d). At first, the oscillating mode of the free carriers gets activated by thermal emission from water. Active electron species start to react with oxygen molecules in water to create super oxide radical anions. Free anion radicals react with diffused hydrogen cations (H^+) in water and yield hydroperoxyl ($HO_2^{\bullet}$) radicals. Subsequently, the hydroperoxyl radicals react with another electron and yield hydrogen peroxide (H_2O_2). At the final stage, new reactive species engage with CB electrons and create $^{\bullet}OH$ radicals that react with adsorbed Rh-B molecules and degrade them into smaller elementary compounds.[78, 83, 84, 87]

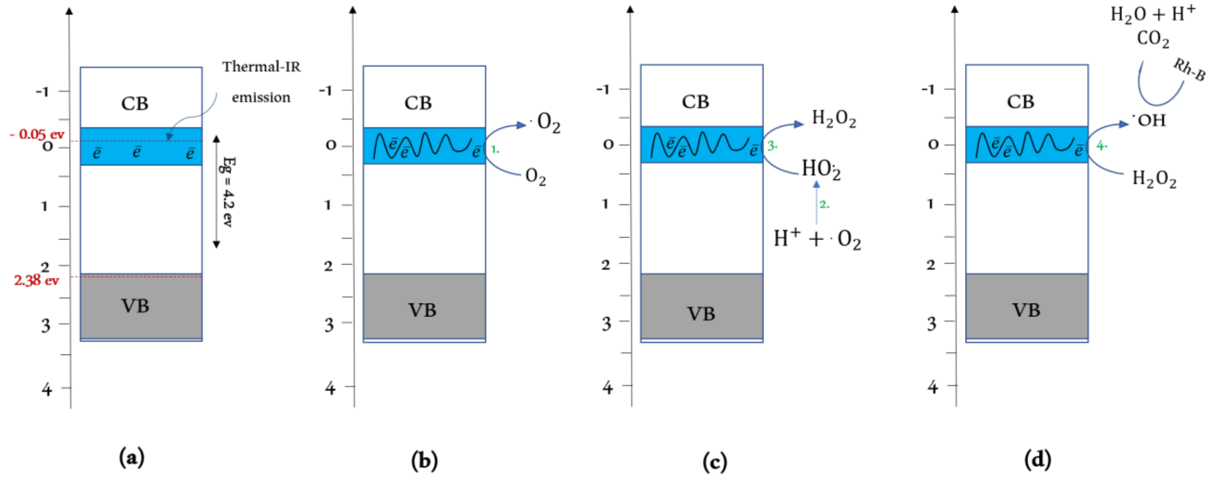

Figure 5.2. Schematic demonstration of proposed Rh-B degradation pathway. (a) The initiation of the LSPR mode *via* thermal-IR emission. (b) The first intermediate step that involves utilizing dissolved O_2 particles in the degradation process. (c) The second and third intermediate steps that involve creating HO_2 and H_2O_2 radicals. (d) Steps leading to the final products of the degradation process.

It is important to point out that according to the demonstrated mechanism in stage (c), H_2O_2 can also be one of the essential steps in the degradation process. Some literature work has been done with $FeCl_2$ where Fe^{3+} gets reduced to Fe^{2+} through the consumption of H_2O_2 according to the formula [88]

$$H_2O_2 + Fe^{2+} \rightarrow \cdot OH + OH^{-} + Fe^{3+} \tag{5.1}$$

Nonetheless, such an argument may not be completely reliable due to the nature of Cl^{-} radicals that allows them to participate in consuming VB holes to create $Cl^{\bullet}$ species.[89]

5.3. Study of sacrificial reagents under UV illumination

Likewise the study of UV with thermal-IR photocatalysis, the trapping experiments were performed under UV illumination for the purpose of confirming some of the aforementioned assumptions and finding the most active species under UV exposure. The scavengers were added at the very beginning of the study and the starting concentration was taken as the dye concentration

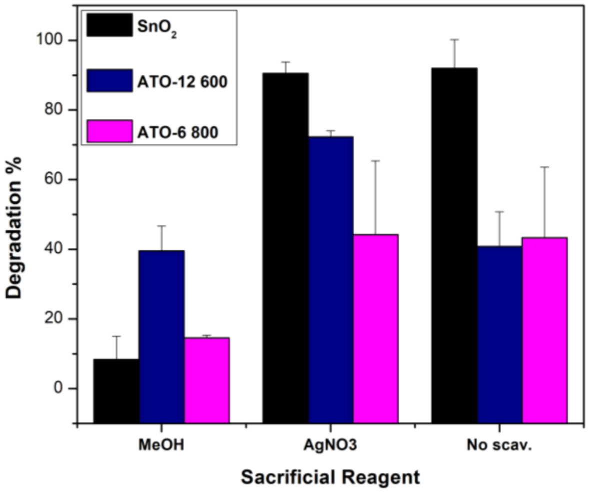

Figure 5.3. Results from performed trapping experiments under UV illumination. The results are compared against those with no scavenger addition.

after 60 minutes of stirring in the dark. This means, the effect of LSPR mode of ATO-12 600 is slightly suppresed or completely eliminated by the capture of the electrons using $AgNO_3$.

Primarly, pure SnO_2 is not affected by the electron scavenger but the activity is significantly reduced when the hole scavenger was used. This observation is consistent with previous reports on SnO_2 indicating that the degradation is hole based. The alignement of the VB of this system allows for an easy utilization of the holes in the degradation process through water reduction.

When it comes to ATO-12 600, the opposite trend is observed and the catalyst is unaffected by MeOH presence and only responds to $AgNO_3$. Since ATO-12 600 photocataytic activity is related to the CB electrons, the material is not expected to show any response to the hole scavenger. The anomaly however, is in the improved activity when $AgNO_3$ was added. Based on the explanation provided in Section 5.1.4 in Chapter 5, ATO-12 600 exhibits a low degradation rate under UV light due to the scattering between LSPR electrons and photogenerated electrons. When the electron scavenger was introduced to the medium prior to UV exposure, LSPR elecrtons were eliminated and thus the photogenerated electrons had a good chance in performing the redox reaction. Therefore, ATO-12 600 became more photocatalytically active under UV illumination in the absence of its LSPR property. Lastly, ATO-6 800 follows the same behavior of pure SnO_2 and is only affected by the addition of the hole scavenger.

5.4. Revisiting the valence band maximum of ATO NPs

Determining the actual potentails of ATO VBM and conduction band maximum (CBM) is a useful tool to correlate observed photocatalytic behavior with quantum mechanical characteristics. Therefore, the XPS data were analyzed at the VB region. Hence, the spectrometer was calibrated with Ag setting the the Fermi level to 0 eV and the samples were in good electrical contact. In order to align the energy potentails against NHE, commercial anatase TiO_2 was also pelletized and scanned with XPS.

The linear extrapolation of the VB edge at the fermi level is presented in Figure 5.4 (a). As can be seen, the VBM shifts downward towards lower energy values with the addition of antimony atoms. Similar observations have been found in the literature; however, the energy shifts were negligible.[69] A plausible explanation of the shift could be the participation from Sb 4d electronic states around 32 eV in which the VBM is constructed of more energy levels and thus, moves closer to the conduction band's minimum.[90, 91] It has been well established in the literature from DFT and photoemission studies that the VBM of SnO_2 is constructed of O 2p, Sn 5s and Sn 5p orbitals.[92] At the shallower and deeper levels, O 2s and Sn 4d start to dominate respectively, with the latter exhibiting a more pronounced and stronger peak due to its higher photoemission cross section.[93,94] Photoemitted VB peaks of SnO_2 are displayed in Figure 5.4 (b). The shift of the peaks toward lower energies with increasing oxygen content, herein achieved by annealing, is consistent with other literature reports on SnO_2.[76]

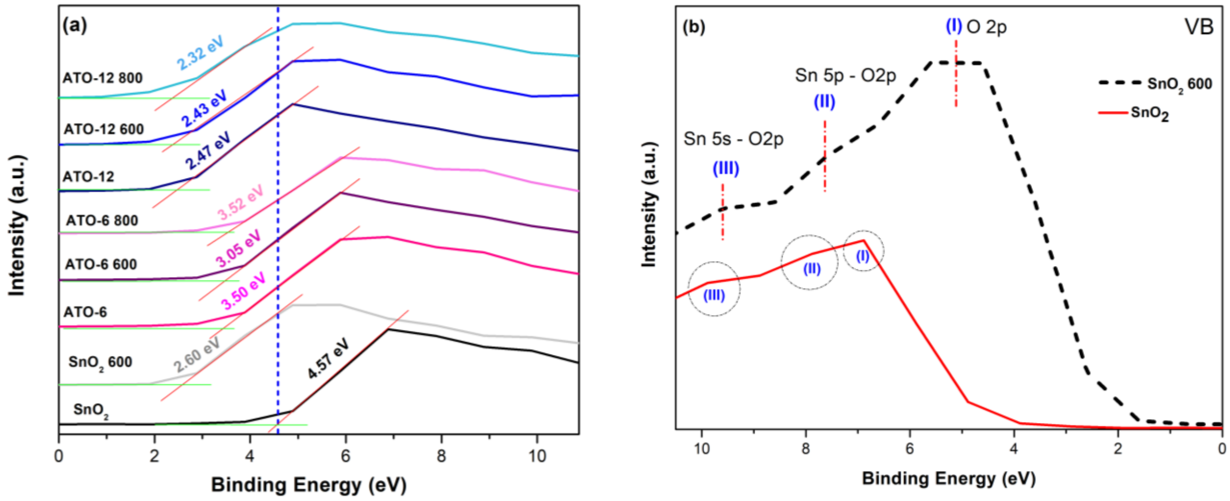

Figure 5.4. (a) Illustration of VB edge linear extrapolation. The dashed blue line is a guide to the eye to show the shift of the VB edge. (b) A display of SnO_2 characteristic VB peaks. The circles

and red dashed lines indicate the position of the satellites that correspond to the assigned orbitals.

As a consequence, the optical band gap may experience some narrowing as the energy from the VBM to CBM gets smaller. However, this is not always the case because of several contributing factors. The CB minimum may get pushed away by the repulsion from the electrons in VBM level which results in higher band gap values. Adding to that, the introduction of more electrons to the CB *via* incorporating Sb^{5+} ions or oxidizing surface aggregated Sb^{3+} to Sb^{5+} will also affect the apparent band gap value. The dual nature of antimony valences complicates the picture even further by the creation of some acceptor states that compensate for the CB electrons and downbends the CB edge.[76] last, from compiled reports, one can infer that surface segregated antimony atoms can generally create a depletion layer at the surface or grain boundaries. [12, 55, 95]

5.5. Aligning SnO_2 and ATO NPs' potentials with NHE

The VB of anatase TiO_2 was found to be about 2.52 eV. This gives a difference of 0.05 to 1 eV between the VBM of anatase and ATO samples. The standard CBM position of TiO_2 is

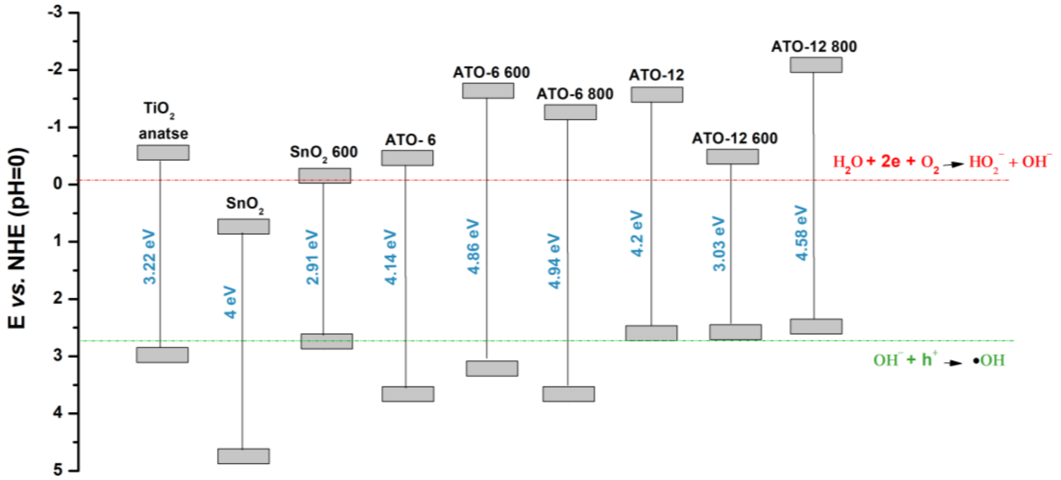

Figure 5.5. Demonstration of the position of the CB and VB potentials with respect to NHE at pH=0.

reported to be -0.4 eV against NHE at pH=0. Taken that the optical band gap of TiO_2 is reported to be 3.22 eV, it was possible to plot the potential of TiO_2 with respect to NHE energy.[69] Also, by knowing the difference between TiO_2 VBM and ATO samples, it was possible to align the potentials with NHE values.

First, the NHE plot supports the observation of reduced SnO_2 600 activity because of annealing. The scavenger results have shown that SnO_2 activity is mainly hole dependent, which gives more importance to the position of its VBM. The potential of SnO_2 was pushed forward above the NHE reduction potential after the annealing, and that consequently lowered the ability of SnO_2 600 to utilize its holes in the degradtion process.

Moreover, the NHE plot further confirms the ability of ATO-12 600 LSPR electrons to participate in the degradation process due to the position of the potential of the CBM. In the general sense, n-doping is expetcted to affect the electronic potentials by the formation of band gap defect states and upward and, possibly, downward shifts of VBM and CB minimum respectively.[96] The potentials of ATO-12 600 complies well with this concept.

The discrepancy in the optical band gap values of SnO_2 600 and ATO-12 600 is not easy to resolve. However, it is important to note that a small band gap value, of about 2.6 eV, has been reported for both SnO_2 and bluish plasmonic ATO NPs in previous studies.[53, 97, 98] Also, it is useful to add that the corresponding band gap values cannot be assigned to bulk SnO, which exhibits a band gap of about 2.7 eV, based on reported XRD data.[99]

The respective shift of the CBM and VBM allowed ATO-6 800 and ATO-12-800 to encompass the water potential which made them ideal for the degradation process; however, the previously stated factors in Section 5.1.2 in the previous chapter rendered the CB electrons useless. The VB potential of ATO-6 800 supports the observation from Figure 5.3 where the degradation process under UV light was hindered by the presence of MeOH. Thereby, the photocatalytic activity of both ATO-6 800 and SnO_2 can be categorized as hole driven processes.

It is clear that no generic explanation can accommodate all of the observed shifts in the potentials, though the assigned positions manifest the accuracy of the assigned photocatalytic activities. The NHE results are in general accordance with the conclusions from the photocatalytic studies.

5.6. Conclusions

A vast majority of photocatalytic studies are stimulated by the global interest in finding safe, cheap and environmentally friendly materials that can be used in water purification. In fact, most of the commercially available applications involve the use of thin films with delicate processing techniques. Before powder catalysts can be utilized, they need to be formulated such that their photocatalytic performance is competitive with already existing systems. Herein, ATO NPs were engineered to perform a photocatalytic response toward thermal-IR excitation using their LSPR property.

In brief, the physical and optical properties of pure and doped SnO_2 samples were outlined through various diffraction, transmission, absorption and photoemission techniques. The investigated samples showed a clear tendency to incorporate antimony atoms at their lower oxidation states due to an ionic radius preference between Sn^{4+} 0.69 A^0 and Sb^{5+} 0.60 A^0. Consequently, the CB density of free carriers gradually increased. This was visually observed by the gradual change of the whitish color of SnO_2 to the greenish color of the doped samples and empirically by the increasing band gap values. The optimum dopant level from this study was found to be 12% antimony dopant concentration.

Thermal treatment was conducted in order to tackle any problems associated with crystallinity and grain boundary aggregation. The main results of the annealing step were the better crystallinity and the higher CB carrier density of the doped samples.

In order to highlight the important parameters involved in thermal-IR photocatalysis, SnO_2 photocatalytic response was investigated in the context of antimony doping and annealing temperature. It is true that accommodating antimony ions in their pentavalent state in the matrix of SnO_2 improves the CB occupancy. This allows the material to display an LSPR feature when excited with a thermal-IR source. However, at low doping concentration, ATO samples were not able to respond to thermal-IR excitation even after the annealing.

As for non-annealed highly doped samples, the active sites were blocked by aggregated antimony atoms that refrained the dye molecules from successfully attaching to the NC. The blockage of the active sites also decreased the system efficiency in responding to UV excitation. In the case of annealed ATO samples, there was a clear sign of thermal-IR response in highly doped samples. ATO-6 600, highly doped ATO 400 and highly doped ATO 600 samples were able to degrade Rh-B in the dark in response to thermal-IR excitation. Moreover, there was a monotonic increase in the degradation activity upon increasing the medium temperature which was also another sign of thermal-IR response. Meanwhile, the integration between LSPR mode and UV radiation can significantly reduce the efficiency of the degradation due to electron scattering.

The degradation mechanism was lastly investigated using trapping experiments. The activity of SnO_2 was hindered by using a hole scavenger which indicates that the reduction of water is the most prevalent reaction in the degradation activity. Explicitly, the hole scavenger showed a minimal engagement in LSPR dependent photocatalysis and the main active species in this type of reactions were electrons and hydroxyl radicals. The removal of LSPR electrons using an electron scavenger allows the system to respond more effectively to UV excitation. The latter finding displays a special importance since the presence of electron scavengers in wastewater can render many of water treatment materials useless or reduce their efficiency.

5.7. Outlooks

Ultimately, there exist different opportunities to improve the photocatalytic performance of ATO samples or to improve the understanding of their thermal-IR response. The behavior of grain boundaries can be spectroscopically proofed by studying the samples with SEM and TEM. Also, the carrier density of the annealed samples can be studied by making transparent thin films of the samples and then exploring their interaction with an IR light using FTIR. Doppler broadening of annihilation radiation spectroscopy combined with an electrical experiment of the resistivity can yield some accurate information about the type and behavior of the defects in the samples. Lastly, detailed analysis of the observed shifts in band gap edges was not within the scope of this project; however, one can work on understanding the relation between photocatalysis and the movement of the band edges against NHE.

One other way to improve the study is to find another synthetic procedure that yields smaller crystallite sizes so that the surface area becomes larger with more surface sites to occupy. In addition, one can work on finding a way to obtain the NPs without aggregating the dopant atoms at the grain boundaries. One last suggestion is to use a surface cleaning method that doesn’t alter the crystallite size and can force aggregated antimony atoms inside the matrix of SnO_2.

Following the same objective of improving the usefulness of powder catalysts for water purification, it is feasible to study the photocatalytic activity of other LSPR systems. Based on the highlighted parameters for thermal-IR response, W, Mo, Nb and Ta represent good candidates if doped with SnO_2. First, their ionic radius allows them to incorporate effectively into the lattice sites of tin atoms. Secondly, all of the suggested elements are commercially available as inexpensive precursors and display high oxidation states which means they can donate their extra electrons to the CB and increase the carrier concentration. More specifically, the carrier density can be improved by a factor of two if W^{6+} got incorporated.

References

(1) González, G. B. *Materials* **2012**, *5*(12), 818–850.

(2) Runnerstrom, E. L.; Llordes, A.; Lounis, S. D.; Milliron, D. J. *Chem. Commun* **2014**, *45* (40), 10555-10572.

(3) Wang, M.; Ye, M.; Iocozzia, J.; Lin, C.; Lin, Z. *Adv. Sci.* **2016**, *3* (1600024), 1-14.

(4) Horikoshi, S; Serpone, N. *Microwaves in nanoparticle synthesis: fundamentals and applications*, 1st ed.; Wiley-VCH Verlag GmbH & Co KGaA: Weinheim: Germany, **2013**.

(5) Unser, S.; Bruzas, I.; He, J.; Sagle, L. *Sensors* **2015**, *15* (7), 15684-15716.

(6) Comin, A.; Manna, L. *Chem. Soc. Rev.* **2014**, *43*, 3957-3975.

(7) Hartland, G. V. *Chem. Rev.* **2011**, *111* (6), 3858–3887.

(8) Toma, H. E.; Zamarion, V. M.; Toma, S. H.; Araki, K. *J. Braz. Chem. Soc.* **2010**, *21*(7), 1158–1176.

(9) Gerard, F. *Advances in plasma physics research.*; Nova Science Publishers: Hauppauge, NY: United States, **2001**.

(10) Wang, T.; Radovanovic, P. V. *J. Phys. Chem. C* **2010**, *115* (2), 406–413.

(11) Khodyuk, I. V.; Quarati, F. G. A.; Alekhin, M. S.; Dorenbos, P. *J. Appl. Phys.* **2013**, *114* (12), 123510.

(12) Shanthi, S.; Subramanian, C.; Ramasamy, P. *J. Cryst. Growth* **1999**, *197* (4), 858-864.

(13) Rao, C. N. R.; Thomas, P. J.; Kulkarni, G. U. *Nanocrystals: synthesis, properties and applications*; Springer: Berlin: Germany, **2011**.

(14) El-Brolossy, T. A.; Abdallah, T.; Mohamed, M. B.; Abdallah, S.; Easawi, K.; Negm, S.; Talaat, H. *Eur. Phys. J. Special Topics* **2008**, *153* (1), 361-364.

(15) Mahmoud, M. A.; Chamanzar, M.; Adibi, A.; El-Sayed, M. A. *J. Am. Chem.*

Soc. **2012**, *134* (14), 6434–6442.

(16) Cuevas, R.; Durán, N.; Diez, M. C.; Tortella, G. R.; Rubilar, O. *J. Nanomater.* **2015**, *16* (1) 1–7.

(17) Naik, G. V.; Shalaev, V. M.; Boltasseva, A. *Adv. Mater.* **2013**, *25* (24), 3258–3258.

(18) Anker, J. N.; Hall, W. P.; Lyandres, O.; Shah, N. C.; Zhao, J.; Duyne, R. P. V. *Nat. Mater.* **2008**, *7*, 442–453.

(19) Park, J.-E.; Kim, S.; Son, J.; Lee, Y.; Nam, J.-M. *Nano Lett.* **2016**, *16* (12), 7962–7967.

(20) Park, J.-E.; Kim, J.; Nam, J.-M. *Chem. Sci.* **2017**, *8* (7), 4696–4704.

(21) Li, Y.; Li, Z.; Chi, C.; Shan, H.; Zheng, L.; Fang, Z. *Adv. Sci.* **2017**, *4* (8), 1600430.

(22) Kudo, A.; Miseki, Y. *Chem. Soc. Rev.* **2009**, *38* (1), 253–278.

Miseki, A. K. and Y. **2009**, No. 1.

(23) Fan, W.; Leung, M. *Molecules* **2016**, *21* (2), 180.

(24) Shi, J.; Shen, S.; Chen, Y.; Shi, J., Shen, S., Chen, Y., Guo, L.; Mao, S. S. *Opt. Express* **2012**, *20* (S2).

(25) Shah, M. W.; Zhu, Y.; Fan, X.; Zhao, J.; Li, Y.; Asim, S.; Wang, C. *Sci. Rep.* **2015**, *5* (1), 1-8.

(26) Zhang, X.; Chen, Y. L.; Liu, R.-S.; Tsai, D. P. *Rep. Prog. Phys.* **2013**, *76*(4), 046401.

(27) Zhang, S.; Li, J.; Wang, X.; Huang, Y.; Zeng, M.; Xu, J. *ACS Appl. Mater. Interfaces* **2014**, *6* (24), 22116–22125.

(28) Zhang, Z.; Wang, W.; Gao, E.; Sun, S.; Zhang, L. *J. Phys. Chem. C* **2012**, *116* (49), 25898–25903.

(29) Yan, J.; Lin, Z.; Ma, C.; Zheng, Z.; Liu, P.; Yang, G. *Nanoscale* **2016**, *8*(32), 15001–15007.

(30) Sun, Y.; Zhao, Z.; Zhang, W.; Gao, C.; Zhang, Y.; Dong, F. *J. Colloid Interface Sci.*

2017, *485*, 1–10.

(31) Pincella, F.; Isozaki, K.; Miki, K. *Light Sci. Appl* **2014**, *3*(1) 1-6.

(32) Newman, B. K.; Sher, M.-J.; Mazur, E.; Buonassisi, T. *Appl. Phys. Lett.* **2011**, *98*(25), 251905.

(33) Tull, B. R.; Winkler, M. T.; Mazur, E. *Appl Phys A* **2009**, *96*(2), 327–334.

(34) Limaye, M. V.; Chen, S. C.; Lee, C. Y.; Chen, L. Y.; Singh, S. B.; Shao, Y. C.; Wang, Y. F.; Hsieh, S. H.; Hsueh, H. C.; Chiou, J. W.; Chen, C. H.; Jang, L. Y.; Cheng, C. L.; Pong, W. F.; Hu, Y. F. *Sci. Rep.* **2015**, *5* (1), 1-12.

(35) Ginley, D.; Hosono, H.; Paine, D. *Handbook of Transparent Conductors*.; Springer Science+Business Media: New York, NY: United States, **2011**.

(36) Chu, D.; Mo, J.; Peng, Q.; Zhang, Y.; Wei, Y.; Zhuang, Z.; Li, Y. *ChemCatChem* **2011**, *3*(2), 371–377.

(37) Rockenberger, J.; Felde, U. Z.; Tischer, M.; Tröger, L.; Haase, M.; Weller, H. *J. Chem. Phys.* **2000**, *112* (9), 4296–4304.

(38) Zhang, L.; Wu, J.; Chen, F.; Li, X.; Schoenung, J. M.; Shen, Q. *J. Asian Ceram. Soc* **2013**, *1*(1), 114–119.

(39) Ahn, J. S.; Pode, R.; Lee, K. B. *Thin Solid Films* **2016**, *608*, 102–106.

(40) Tran, H. A.; Rananavare, S. B. (2011, Aug 15-18). Synthesis and Characterization of N- and P- Doped Tin Oxide. *11th IEEE International Conference on Nanotechnology*. Portland: IEEE

(41) Luo, H.; Fang, Z.; Song, N.; Garvey, T.; Lopez, R.; Meyer, T. J. *ACS Appl. Mater. Interfaces* **2015**, *7* (45), 25121–25128.

(42) Bai, Y.; Fang, Y.; Deng, Y.; Wang, Q.; Zhao, J.; Zheng, X.; Zhang, Y.; Huang, J. *ChemSusChem* **2016**, *9* (18), 2686–2691.

(43) Viet, P. V.; Thi, C. M.; Hieu, L. V. *J. Nanomater.* **2016**, *4231046*, 1–8.

(44) Elango, G.; Roopan, S. M. *J. Photochem. Photobiol., B* **2016**, *155*, 34–38.

(45) Bhattacharjee, A.; Ahmaruzzaman, M. *J. Colloid Interface Sci.* **2015**, *448*, 130–139.

(46) Cheng, G.; Chen, J.; Ke, H.; Shang, J.; Chu, R. *Mater. Lett.* **2011**, *65* (21-22), 3327–3329.

(47) Babu, B.; Kadam, A.; Ravikumar, R.; Byon, C. *J. Alloys Compd.* **2017**, *703*, 330–336.

(48) Chandran, D.; Nair, L. S.; Balachandran, S.; Babu, K. R.; Deepa, M. *J Sol-Gel Sci Technol* **2015**, *76*(3), 582–591.

(49) Saravanakumar, K.; Muthuraj, V. *Optik* **2017**, *131*, 754–763.

(50) Wu, W.; Liao, L.; Zhang, S.; Zhou, J.; Xiao, X.; Ren, F.; Sun, L.; Dai, Z.; Jiang, C. *Nanoscale* **2013**, *5*(12), 5628.

(51) Khan, M. M.; Ansari, S. A.; Khan, M. E.; Ansari, M. O.; Min, B.-K.; Cho, M. H. *New J. Chem.* **2015**, *39* (4), 2758–2766.

(52) Al-Hamdi, A. M.; Sillanpää, M.; Dutta, J. *Appl. Surf. Sci.* **2016**, *370*, 229–236.

(53) Rawal, S. B.; Chakraborty, A. K.; Kim, Y. J.; Kim, H. J.; Lee, W. I. *RSC Adv.* **2012**, *2* (2), 622–630.

(54) Geraldo, V.; Scalvi, L. V. D. A.; Morais, E. A. D.; Santilli, C. V.; Pulcinelli, S. H. *Mater. Res.* **2003**, *6*(4), 451–456.

(55) Felde, U. Z.; Haase, M.; Weller, H. *J. Phys. Chem. B* **2000**, *104* (40). 9388-9395.

(56) Oakton, E.; Tillier, J.; Siddiqi, G.; Mickovic, Z.; Sereda, O.; Fedorov, A.; Copéret, C. *New J. Chem.* **2016**, *40* (3), 2655–2660.

(57) Yadav, A. A.; Pawar, S.; Patil, D.; Ghogare, M. *J. Alloys Compd.* **2015**, *652*, 145–152.

(58) Esro, M.; Georgakopoulos, S.; Lu, H.; Vourlias, G.; Krier, A.; Milne, W. I.; Gillin, W. P.; Adamopoulos, G. *J. Mater. Chem. C.* **2016**, *4* (16), 3563–3570.

(59) Zhang, J.; Gao, L. *Inorg. Chem. Commun* **2004**, *7*, 91–93.

(60) Müller Vesna; Rasp, M.; Štefanić Goran; Ba, J.; Günther Sebastian; Rathousky, J.; Niederberger, M.; Fattakhova-Rohlfing, D. *Chem. Mater.* **2009**, *21* (21), 5229–5236.

(61) Li, N.; Meng, Q. (2010, August 26). Synthesis and characterization of antimony-doped tin oxide (ATO) nanoparticles. Advances in Energy Engineering (ICAEE). Beijing, China: IEEE

(62) Zheng, M.; Wang, B. *Trans. Nonferrous Met. Soc. China* **2009**, *19* (2), 404–409.

(63) Xu, J. M.; Li, L.; Wang, S.; Ding, H. L.; Zhang, Y. X.; Li, G. H. *CrystEngComm* **2013**, *15* (17), 3296.

(64) Cui, G.; Wang, W.; Ma, M.; Xie, J.; Shi, X.; Deng, N.; Xin, J.; Tang, B. *Nano Lett* **2015**, *15*(11), 7199–7203.

(65) Çengel. Y. *Heat transfer a practical approach.*; McGraw-Hill: Boston, Mass: United States, 2006.

(66) Benelmekki, M. *Designing hybrid nanoparticles*; Morgan & Claypool Publishers: San Rafael, CA: United States, 2015.

(67) Ghodsi, V.; Jin, S.; Byers, J. C.; Pan, Y.; Radovanovic, P. V. *J. Phys. Chem. C* **2017**, *121* (17), 9433–9441.

(68) Uddin, J. *Macro To Nano Spectroscopy.;* InTech: Rijeka: Croatia, 2012.

(69) Yang, L.; Huang, J.; Shi, L.; Cao, L.; Zhou, W.; Chang, K.; Meng, X.; Liu, G.; Jie, Y.; Ye, J. *Nano Energy* **2017**, *36*, 331–340.

(70) Rechberger, F.; Ilari, G.; Niederberger, M. *Chem. Commun.***2014**, *50* (86), 13138–13141.

(71) Ávila-Vázquez, V.; Galván-Valencia, M.; Ledesma-García, J.; Arriaga, L. G.; Collins-Martínez, V. H.; Guzmán-Martínez, C.; Escalante-Garcia, I. L.; Durón-Torres, S. M. *J Appl Electrochem* **2015**, *45* (11), 1175–1185.

(72) Egdell, R.; Flavell, W.; Tavener, P. *J. Solid State Chem.* **1984**, *51* (3), 345–354.

(73) Luo, S.; Chu, P. K.; Liu, W.; Zhang, M.; Lin, C. *Appl. Phys. Lett.* **2006**, *88* (18), 183112.

(74) Fang, H.; Radovanovic, P. (2017). *Manipulation of the plasmonic properties of n-type doped colloidal indium oxide nanocrystals.* (Master's thesis). University of Waterloo, Waterloo, Canda

(75) Fang, H.; Hegde, M.; Yin, P.; Radovanovic, P. V. *Chem. Mater.* **2017**, *29* (11), 4970-4979.

(76) Körber, C.; Ágoston, P.; Klein, A. *Sens. Actuators, B* **2009**, *139* (2), 665–672.

(77) Babar, A. R.; Shinde, S. S.; Moholkar, A. V.; Bhosale, C. H.; Kim, J. H.; Rajpure, K. Y. *J. Semicond.* **2011**, *32* (5), 053001.

(78) Kim, S. P.; Choi, M. Y.; Choi, H. C. *Mater. Res. Bull* **2016**, *74*, 85–89.

(79) Mao, W.; Xiong, B.; Liu, Y.; He, C. *Appl. Phys. Lett.* **2013**, *103* (3), 031915.

(80) Mao, W.; Xiong, B.; Li, Q.; Zhou, Y.; Yin, C.; Liu, Y.; He, C. *Phys. Lett. A* **2015**, *379* (36), 1946–1950.

(81) Shokr, E. K. *Semicond. Sci. Technol* **2000**, *15* (3), 247–253.

(82) Prakash, K.; Kumar, P. S.; Pandiaraj, S.; Saravanakumar, K.; Karuthapandian, S. *J. Exp. Nanosci* **2016**, *11* (14), 1138–1155.

(83) Zhuang, S.; Xu, X.; Pang, Y.; Hu, J.; Yang, C.; Tong, L.; Zhou, Y. *RSC Adv* **2013**, *3* (43), 20422–20428.

(84) Du, D.; Li, W.; Chen, S.; Yan, T.; You, J.; Kong, D. *New J. Chem* **2015**, *39* (4), 3129–3136.

(85) Tan, H. L.; Wen, X.; Amal, R.; Ng, Y. H. *J. Phys. Chem. Lett* **2016**, *7* (7), 1400–1405.

(86) Zheng, P.; Pan, Z.; Li, H.; Bai, B.; Guan, W. *J Mater Sci: Mater Electron* **2015**, *26* (9), 6399–6410.

(87) Lee, W. W.; Lu, C.-S.; Chuang, C.-W.; Chen, Y.-J.; Fu, J.-Y.; Siao, C.-W.; Chen, C.-

C. *RSC Adv* **2015**, *5* (30), 23450–23463.

(88) Zhang, J.; Nosaka, Y. *The J. Phys. Chem.C* **2013**, *117*(3), 1383–1391.

(89) Surolia, P. K.; Tayade, R. J.; Jasra, R. V. *Ind. Eng. Chem. Res.* **2007**, *46* (19), 6196–6203.

(90) Zhou, W.; Liu, Y.; Yang, Y.; Wu, P. *J. Phys. Chem. C* **2014**, *118* (12), 6448–6453.

(91) Kato, D.; Hongo, K.; Maezono, R.; Higashi, M.; Kunioku, H.; Yabuuchi, M.; Suzuki, H.; Okajima, H.; Zhong, C.; Nakano, K.; Abe, R.; Kageyama, H. *J. Am. Chem. Soc* **2017**, *139* (51), 18725–18731.

(92) Weidner, M.; Klein, A.; Ensinger, W. (2016). *Fermi Level Determination in Tin Oxide by Photoelectron Spectroscopy: Relation to Optoelectronic Properties; Band Bending at Surfaces and Interfaces; Modulation Doping.* (Doctoral dissertation). Technische Universität Darmstadt, Darmstadt, Germany

(93) Farahani, S. K. V.; Veal, T. D.; Mudd, J. J.; Scanlon, D. O.; Watson, G. W.; Bierwagen, O.; White, M. E.; Speck, J. S.; Mcconville, C. F. *Phys. Rev. B: Condens. Matter* **2014**, *90* (15), 155413.

(94) Cox, P.; Egdell, R.; Harding, C.; Patterson, W.; Tavener, P. *Surf. Sci. Lett.* **1982**, *123* (2-3), 179-203.

(95) Ke, C.; Zhu, W.; Zhang, Z.; Tok, E. S.; Ling, B.; Pan, J. *Sci. Rep.* **2015**, *5* (1), 17424.

(96) Brokken-Zijp, J. C. M.; Asselen, O. L. J. V.; Kleinjan, W. E.; Belt, R. V. D.; With, G. D. *J Nanotechnol* **2011**, *2011*, 106254.

(97) Aqili, A. K. S.; Shah, N. A.; Ali, A.; Maqsood, A. (2006). *Effect of antimony doping on the structure, electrical and optical properties of TIN oxide thin films: Prooceedings of the International Symposium on Advanced Materials.* (pp.420-424). Islamabad: Sci. Int. (Lahore).

(98) Manifacier, J.; Murcia, M. D.; Fillard, J.; Vicario, E. *Thin Solid Films* **1977**, *41* (2), 127–

135.

(99) Peng, H.; Bikowski, A.; Zakutayev, A.; Lany, S. *APL Materials* **2016**, *4* (10), 106103.

Appendix A

Chapter 3 related supplementary information

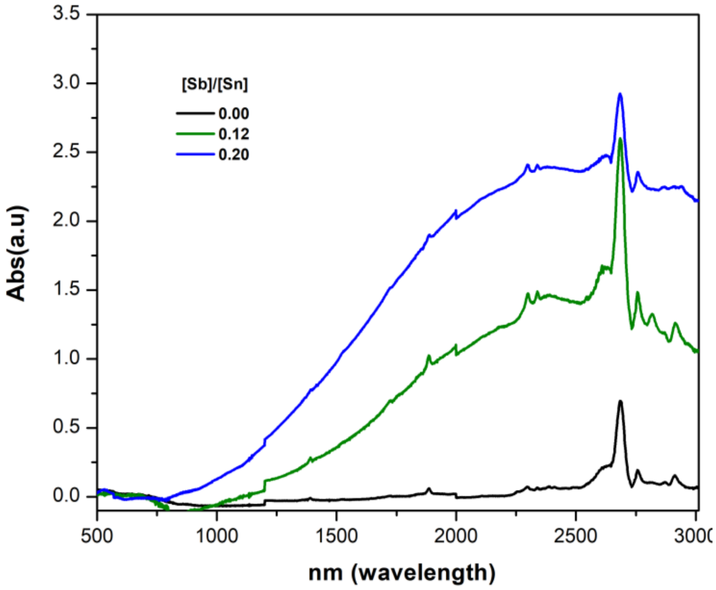

Figure A.1. Demonstration of the change in the plasmonic peak intensity of ATO-12 and ATO-20. The powder was dispersed in perchloroethylene with the addition of a few drops of oleylamine.

Appendix B

Chapter 4 related supplementary information

Table.B.1 Summary of SnO_2 crystallite size determined by Scherrer equation

Treatment Condition	δ (nm)
As-synthesized	10.10
Annealed at 400 ℃	10.56
Annealed at 600 ℃	19.14
Annealed at 800 ℃	29.91

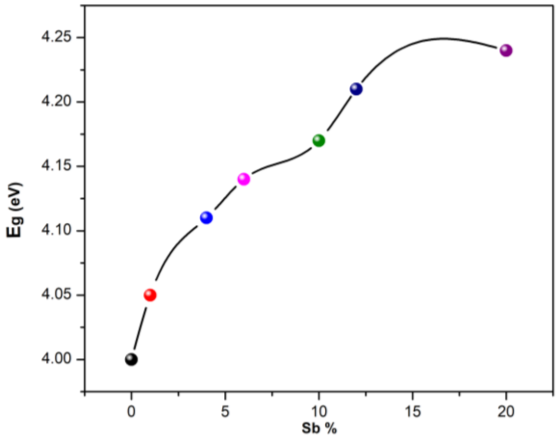

Figure B.1. Band gap trend as a function of antimony nominal concentration.The solid line is a guide to the eye.

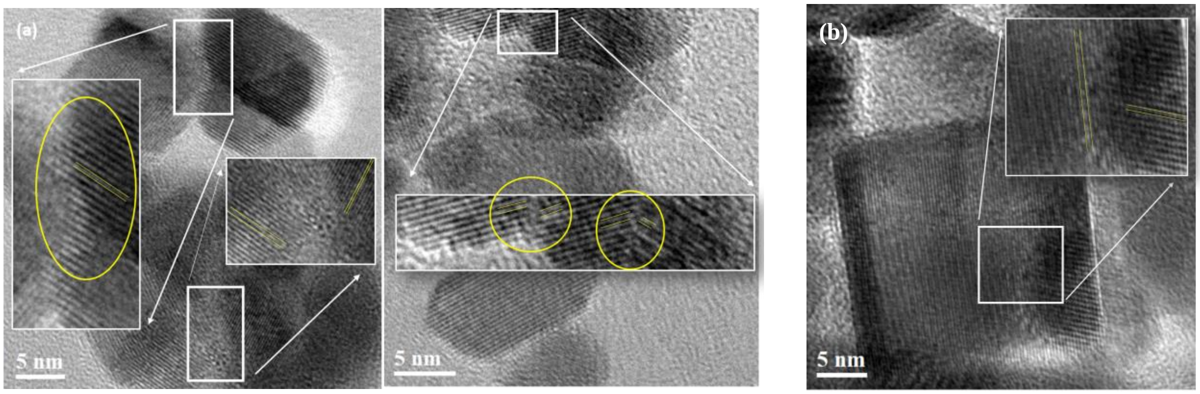

Figure B.2. Display of grain boundaries in as-synthesized (a) SnO_2 NCs. (b) ATO-12 NCs.

Appendix C

Chapter 5 related supplementary information

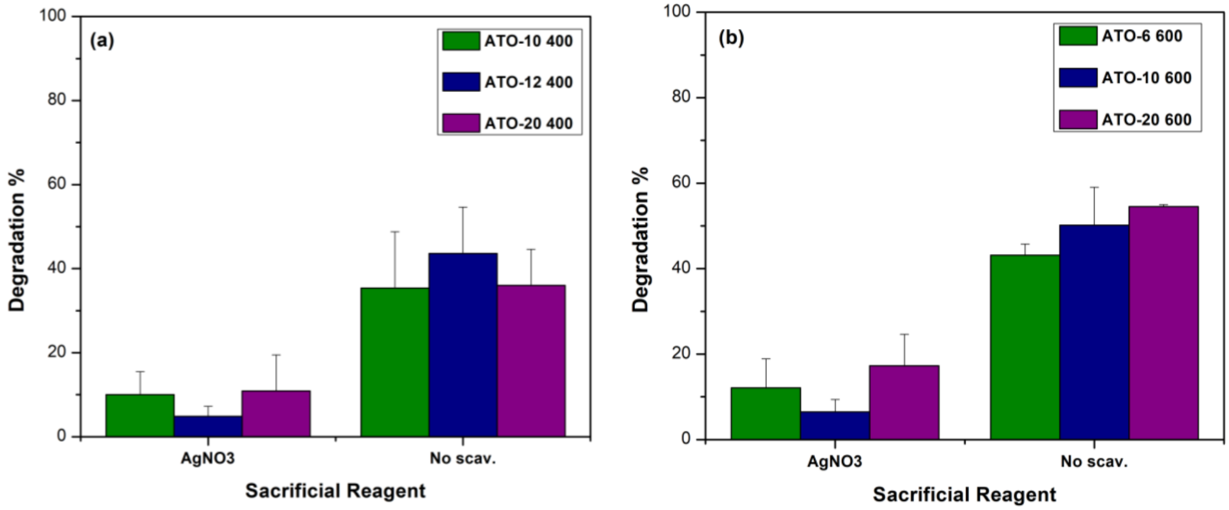

Figure C.1. Results from trapping experiments using $AgNO_3$ as an electron scavenger. The results are compared against those with no scavenger addition. Panel (a) Active ATO 400 samples. (b) Active ATO 600 samples.

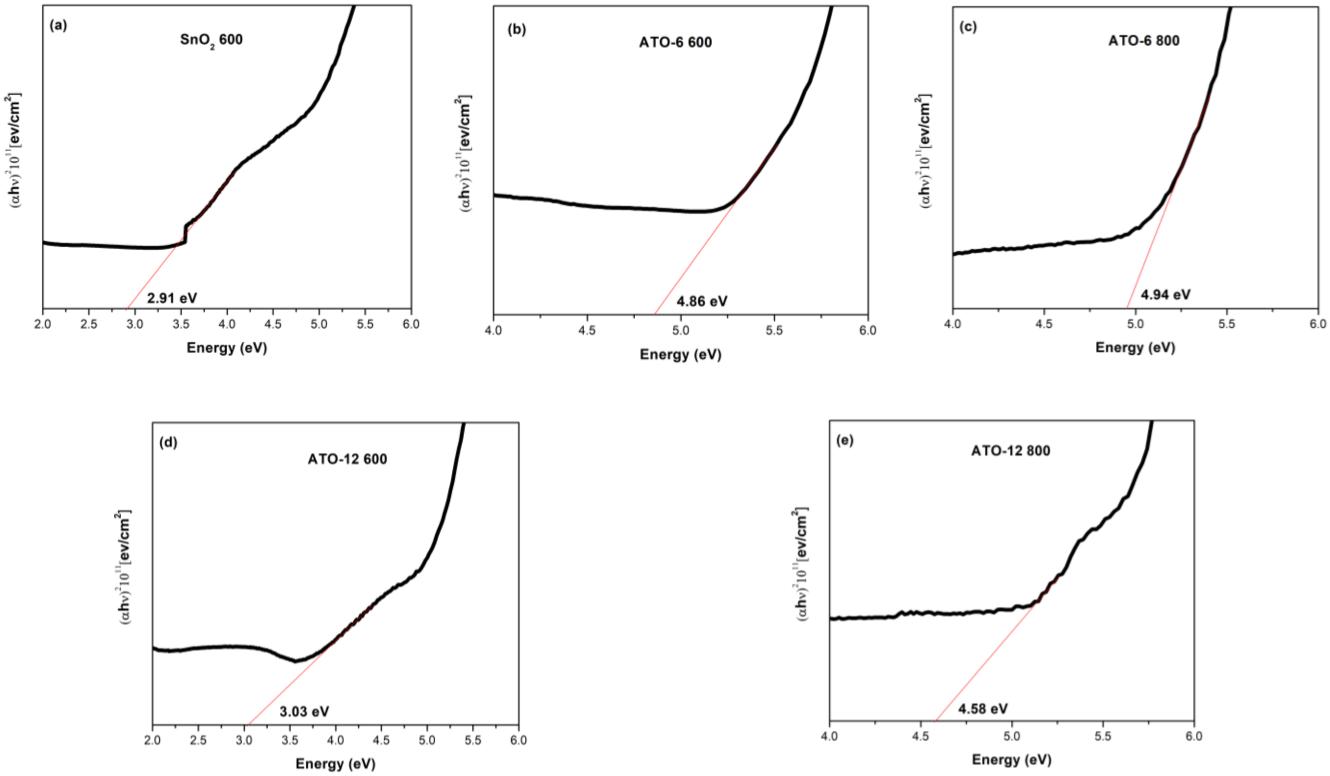

Figure C.2. Tauc plot of annealed samples for optical band gap extrapolation. Powder samples were dispersed in cyclohexane, sonicated for 30 minutes and immediately deposited on a quartz substrate. (a) SnO_2 600. (b) ATO-6 600. (c) ATO-6 800. (d) ATO-12 600. (e) ATO-12 800.

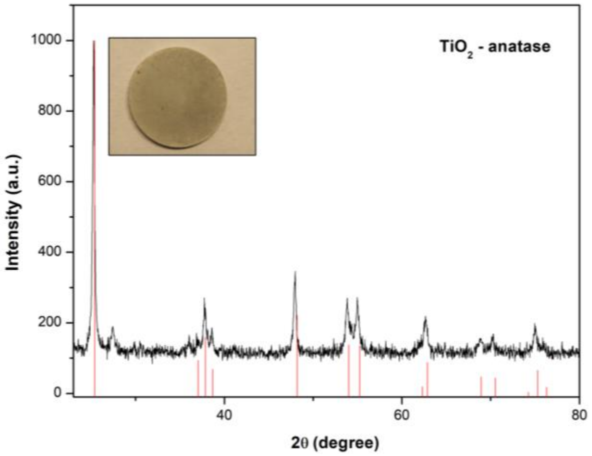

Figure C.3. XRD diffraction peaks for commercial anatase TiO_2. The caption shows a digital photograph of pelletized TiO_2.